Simultaneous Assimilation of Planetary Boundary Layer Observations from Radar and All-Sky Satellite Observations to Improve Forecasts of Convection Initiation

KEENAN C. EURE,[a] PAUL D. MYKOLAJTCHUK,[a] YUNJI ZHANG,[a] DAVID J. STENSRUD,[a] FUQING ZHANG,[a] STEVEN J. GREYBUSH,[a] AND MATTHEW R. KUMJIAN[a]

[a] *Department of Meteorology and Atmospheric Science, The Pennsylvania State University, University Park, Pennsylvania*

(Manuscript received 14 July 2022, in final form 3 November 2022)

ABSTRACT: Accurate predictions of the location and timing of convection initiation (CI) remain a challenge, even in high-resolution convection-allowing models (CAMs). Many of the processes necessary for daytime CI are rooted in the planetary boundary layer (PBL), which numerical models struggle to accurately predict. To improve ensemble forecasts of the PBL and subsequent CI forecasts in CAM ensembles, we explore the use of underused data from both the *GOES-16* satellite and the national network of WSR-88D radars. The *GOES-16* satellite provides observations of brightness temperature (BT) to better analyze cloud structures, while the WSR-88D radars provide PBL height estimates and clear-air radial wind velocity observations to better analyze PBL structures. The CAM uses the Advanced Research Weather Research and Forecasting (WRF-ARW) Model at 3-km horizontal grid spacing. The ensemble consists of 40 members and observations are assimilated using the Gridpoint Statistical Interpolation (GSI) ensemble Kalman filter (EnKF) system. To evaluate the influence of each observation type on CI, conventional, WSR-88D, and *GOES-16* observations are assimilated separately and jointly over a 4-h period and the resulting ensemble analyses and forecasts are compared with available observations for a CI event on 18 May 2018. Results show that the addition of the WSR-88D and *GOES-16* observations improves the CI forecasts out several hours in terms of timing and location for this case.

SIGNIFICANCE STATEMENT: The location and timing of new thunderstorm development is an important component of severe weather forecasts. Yet the prediction of thunderstorm development in weather prediction models remains challenging. This study explores using a combination of underused satellite and radar observations to better define the atmospheric state used to start the weather prediction models, with the hope that this will lead to better forecasts of new thunderstorm development. Results show that underused observations from routinely available Doppler weather radars and a geostationary satellite, all of which are currently available, can work synergistically to improve forecasts of the location and timing of severe thunderstorm development.

KEYWORDS: Boundary layer; Radars/Radar observations; Satellite observations; Mesoscale forecasting; Data assimilation; Mesoscale models

1. Introduction

Since 1980, severe thunderstorms have accounted for over $344.8 billion in damages and 1972 deaths nationwide (NOAA/National Centers for Environmental Information 2022). Given the lives lost and property damaged, accurate predictions of severe convection and their associated hazards are critical to operational weather forecasting. Advances in computational resources, observation platforms and capabilities, numerical weather prediction models (NWPs), and data assimilation techniques have improved detection and forecasts of severe weather hazards over time (Stensrud et al. 2013), but accurate prediction of convection initiation (CI) remains a challenge (Kain et al. 2013). Moisture, lift, and instability—the three ingredients needed for CI (Johns and Doswell 1992)—often are not well represented in models and these inaccuracies likely contribute to the difficulties of CI prediction.

Near-surface moisture, lift, and instability, as well as temperature and winds, are strongly influenced by planetary boundary layer (PBL) structure, thereby making CI very sensitive to the evolution of the PBL (Crook 1996; McCaul and Cohen 2002; Martin and Xue 2006; Sobash and Stensrud 2015; Hu et al. 2019). Model forecasts that do not initiate convection at the correct location and time can have negative feedbacks on model variables in response to inaccurate convective prediction (Brooks et al. 1994; Stensrud 1996; Kerr et al. 2019). Therefore, accurate prediction of ongoing convection as well as PBL structure is critical for convection forecasts (Johnson and Mapes 2001; Browning et al. 2007).

Several approaches have been used to incorporate ongoing convection in model initial conditions using Doppler radar observations of radar reflectivity factor (hereafter reflectivity) and radial velocity, including a cloud analysis (Hu et al. 2006), three-dimensional variational approaches (Gao et al. 1999; Crook and Sun 2002; Wu et al. 2002; Dixon et al. 2009), four-dimensional variational approaches (Sun 2005; Sun and Zhang 2008), and ensemble-based methods (Snyder and Zhang 2003; Dowell et al. 2004; Tong and Xue 2005; Aksoy et al. 2009; Yussouf et al. 2013). Results from these studies demonstrate the benefits of an accurate depiction

F. Zhang: Deceased

Corresponding author: Keenan C. Eure, kce115@psu.edu

DOI: 10.1175/MWR-D-22-0188.1

of ongoing convection to the prediction of its subsequent evolution.

Observations from the *GOES-16*, operational in 2017, present unique opportunities for improved CI prediction. The Advanced Baseline Imager (ABI) instrument of this satellite allows for scans of the continental United States (CONUS) every 5 min. For infrared channels, the spatial resolution is 2 km, sufficient for visualizing the development of convection (Schmit et al. 2017). The availability of new satellites with more frequent observations at finer resolution has increased the use of satellite observations in convection-allowing models (CAMs; Zou et al. 2013; Jones et al. 2015, 2020; Zhang et al. 2016; Cintineo et al. 2016; Minamide and Zhang 2018; Zhang et al. 2019). Zhang et al. (2018, 2019), Jones et al. (2020), Minamide and Posselt (2022), and Johnson et al. (2022) illustrate success in the prediction of isolated supercell storms when assimilating all-sky radiances from the *GOES-16* ABI. Several operational centers are moving toward assimilating cloudy radiances, in addition to clear-sky radiances (e.g., Geer et al. 2018). The assimilation of satellite observations is effective in removing precipitating and nonprecipitating clouds in models where they are not observed, and vice versa. The addition of satellite observations can improve upon forecasts initialized with Doppler radar observations (Jones et al. 2015, 2020) as well as providing information regarding ongoing convection where radar observations are unavailable.

Clear-air Doppler radar and other remote sensing observations can be incorporated into model initial conditions to better depict PBL structure. Accurate depictions of PBL winds are particularly important for CI, as drylines, airmass boundaries, and outflow boundaries all provide lift that contributes to storm development (Weckwerth and Parsons 2006). Improved characterization of these features in the PBL can be gained from use of radial velocity observations (Xu et al. 1995). While WSR-88D radial velocity observations have been assimilated within storms when the reflectivity is ≥20 dBZ to improve depictions of wind fields (Snyder and Zhang 2003; Aksoy et al. 2009; Wheatley et al. 2015; Yussouf et al. 2015), clear-air radial velocities also are routinely available prior to CI. However, they are often assimilated only as a single vertical wind profile at each radar, calculated using the velocity–azimuth display (VAD) method (Browning and Wexler 1968). Clear-air radial velocities are shown to improve the pre-CI PBL winds in observing system simulation experiments (Zhang et al. 2009; Huang et al. 2020, 2022).

Hu et al. (2019) assimilate Atmospheric Emitted Radiance Interferometer (AERI) temperature and mixing ratio profiles, Doppler lidar VAD wind profiles, and WSR-88D clear-air VAD wind profiles to obtain improved PBL structures during the daytime, leading to improved CI forecasts, while Degelia et al. (2019) find similar results from assimilating ground-based remote sensing observations at night. Tangborn et al. (2021) and Dang et al. (2022) assimilate lidar backscatter retrievals of PBL height to improve PBL forecasts, as PBL height is a key parameter defining the PBL yet forecasts of PBL height can differ from observations by a factor of 2 (Grimsdell and Angevine 1998; Bright and Mullen 2002; Stensrud and Weiss 2002). In both studies, the assimilation had the largest impact in the daytime. These results highlight the benefit of remotely sensed observations within the PBL for improving PBL depiction and subsequent forecasts of CI. To our best knowledge, PBL height observations are not assimilated in operational models, and prior research warrants further exploration into the use of these routine observations.

Much of the recent work assimilating both radar and satellite observations has been accomplished using the ensemble Kalman filter (EnKF; Evensen 1994; Houtekamer and Zhang 2016). The EnKF provides flow-dependent background error covariances and has been widely used for improving severe thunderstorm forecasts in CAMs (e.g., Snyder and Zhang 2003; Aksoy et al. 2009; Jones et al. 2016, 2020; Zhang et al. 2018, 2019). Results from Johnson et al. (2015) suggest that the ensemble Kalman filter approach yields precipitation forecasts that are more skillful than those from a three-dimensional variational approach. The Warn-on-Forecast System (WoFS; Stensrud et al. 2009, 2013; Gallo et al. 2017) uses EnKF data assimilation with observations assimilated every 15 min, allowing for a relatively high-temporal-resolution assimilation to generate short-term forecasts (0–6 h) of high-impact weather events. Ensemble data assimilation has shown success in linking all-sky radiances with the model temperature, water vapor, and wind fields (Houtekamer and Zhang 2016).

This exploratory study assimilates infrared brightness temperatures (BTs) from the *GOES-16*, in conjunction with clear-air radial wind and PBL height from the WSR-88Ds, to better represent ongoing convection and PBL structures in the CAM ensemble initial conditions and to evaluate if these observations improve daytime CI forecasts. To our best knowledge, observations of radar-estimated PBL height, preconvective PBL winds from radars, and all-sky radiances from geostationary satellites, are not assimilated in any operational model. The focus in this work is to simultaneously assimilate satellite and radar observations *prior* to CI and understand how these observations subsequently influence CI several hours later. Section 2 provides a summary of the selected event on 18 May 2018, while section 3 provides details on the numerical weather prediction model, assimilation method, observations, and data assimilation experiments. The experiment results are discussed in section 4, which explores different combinations of radar and satellite data assimilated (separately and jointly), followed by a summary in section 5.

2. Overview of 18 May 2018 case

At 1800 UTC 18 May 2018, a surface low is present in southeast Colorado, with a quasi-stationary front extending eastward into central Kansas (Fig. 1). The dryline progresses steadily eastward throughout the day, and at 1900 UTC is observed to the east of the Texas–New Mexico border (Fig. 1), stretching south from the center of the low. There is some elevated convection that forms near Lubbock, Texas, around 1800 UTC, that moves northeast and reaches the southeastern corner of the Texas Panhandle at 2200 UTC (Fig. 2a). Eastward propagation and mixing of the dryline act to create lift within an environment in which surface-based convection could develop.

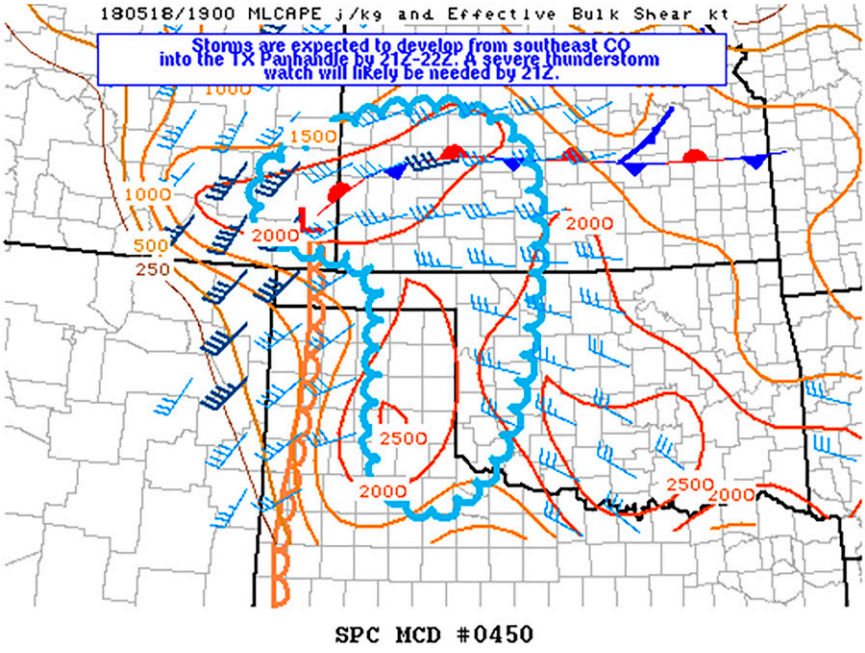

FIG. 1. NOAA Storm Prediction Center's Mesoscale Discussion 0450 from 1900 UTC 18 May 2018, depicting the dryline (orange half-circles), effective bulk shear (in knots, 1 kt $\approx$ 0.51 m s^{-1}; light and navy blue), mean-layer convective available potential energy (MLCAPE; in J kg^{-1}; solid orange contours), quasi-stationary front (blue triangles and red half-circles), and the center of the low pressure system (red L).

Per the NOAA Storm Prediction Center (SPC), the primary threats in the Texas and Oklahoma Panhandles are damaging winds and large hail. A severe thunderstorm watch is issued at 1935 UTC covering far western Oklahoma and the eastern Texas Panhandle. For the CI that is the focus of this study, isolated storms develop in the northeastern Texas Panhandle between 2100 and 2200 UTC, the first forming just east of Amarillo, Texas (Fig. 2b). Over the next hour, storms continue to develop along a north–south line that stretches from the northeastern Texas Panhandle across the Oklahoma Panhandle. After 2300 UTC, additional storms form to the east along the outflow boundaries created by the original convection, leading to a larger multicellular convective cluster by 0000 UTC (Fig. 2c). The broad convective cluster in the Texas

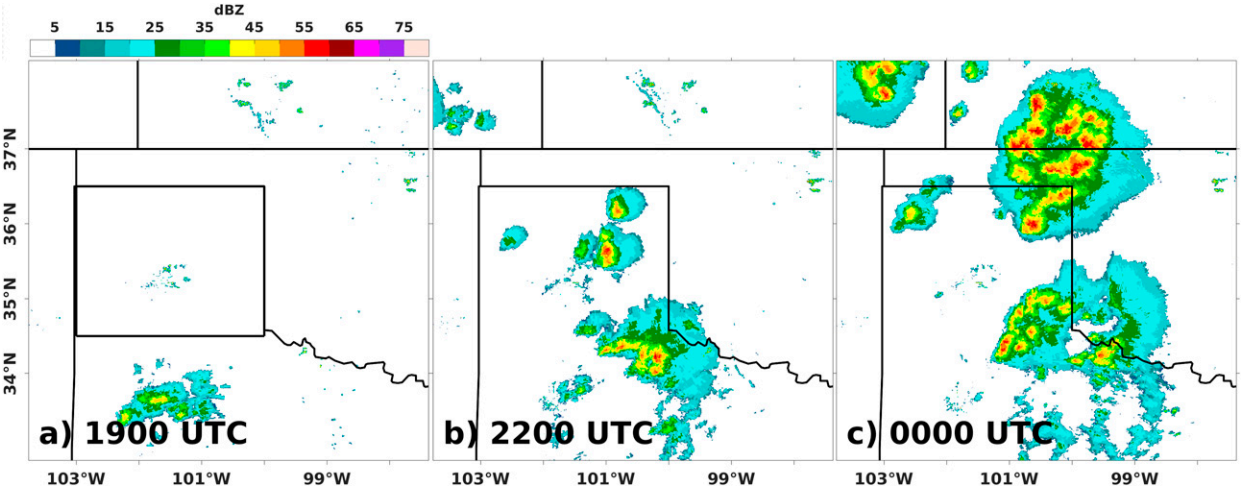

FIG. 2. Observed composite reflectivity (in dBZ, shaded according to outset color bar) at (a) 1900 UTC 18 May, (b) 2200 UTC 18 May, and (c) 0000 UTC 19 May 2018. The area of the figure depicts the model domain, and the black box in (a) outlines the smaller region used to focus on CI.

and Oklahoma Panhandles produces large hail and dozens of damaging wind reports.

3. Methods

a. Numerical model

The High-Resolution Rapid Refresh (HRRR) configuration (Benjamin et al. 2016) of the Advanced Research Weather Research and Forecasting (WRF-ARW) Model (Skamarock et al. 2008) version 3.8.1, is used for the CAM ensemble forecasts. The top of the model is at 50 hPa and it has a single domain of 200 × 200 × 51 grid points. The simulations all have horizontal grid spacing of 3 km. The domain includes portions of eastern New Mexico, southeastern Colorado, and southern Kansas (Fig. 2a). A large portion of the domain is northern and western Texas and western Oklahoma—where the convection formed in their respective panhandles. Physical parameterizations in this study mirror those of the operational HRRR configuration of the WRF-ARW. For PBL and surface processes, the Mellor–Yamada–Nakanishi–Niino (MYNN) 2.5-level turbulent kinetic energy (TKE) scheme (Nakanishi and Niino 2006, 2009; Olson et al. 2019) is used with the Rapid Update Cycle land surface model (Benjamin et al. 2004). The Rapid Radiative Transfer Model for general circulation models (RRTMG; Iacono et al. 2008) is selected for the parameterization of longwave and shortwave radiation. The Thompson et al. (2008) microphysics scheme is used, providing mass mixing ratios of hydrometeors as well as simulated S-band reflectivity.

To create the 40-ensemble member initial conditions, two 20-member ensemble forecasts from the 0000 and 0600 UTC 18 May 2018 Global Ensemble Forecast System (GEFS) analyses are run forward to 0000 UTC 19 May 2018. A slightly larger model domain (10% outward) is used to allow enough space outside of the model domain's boundaries, while keeping the outermost grid points of the input simulations away from the output domain. For each set of 20 ensemble members, the 1200 UTC means of each set are subtracted from all the forecast outputs from 1200 to 0000 UTC of the next day. These 12-h perturbations are added back to the HRRR analysis at 1200 UTC, and these recentered forecasts are used as initial and boundary conditions for the EnKF experiments. Additional random perturbations to soil temperature, soil moisture, and vegetation fraction are used in the ensemble members, as in Zhang et al. (2018, 2019).

b. Data assimilation approach

The community version of the Gridpoint Statistical Interpolation (GSI; version 3.7) based EnKF (version 1.3) system, (Wu et al. 2002; Kleist et al. 2009; Wang et al. 2013; Wang and Lei 2014; Johnson et al. 2015; Liu et al. 2018) extended to ingest satellite radiances, (Jones et al. 2020; Johnson et al. 2022) is used to assimilate observations. This version includes an ensemble square root filter (Whitaker and Hamill 2002).

Relaxation to prior perturbation is applied (Zhang et al. 2004), where 80% of prior perturbations and 20% of posterior perturbations spread is used to maintain suitable ensemble spread throughout cycling. Multiplicative inflation of 10% (Anderson and Anderson 1999) is used on the background ensemble forecasts to increase spread for GSI to better ingest the observations. The GSI EnKF updates the standard atmospheric variables, including hydrometeors, but does not update land surface variables such as soil moisture and soil temperature.

c. Observations for assimilation

1) Brightness temperatures from *GOES-16* ABI

The *GOES-16* ABI is a passive instrument that measures visible and infrared radiances in 16 specific wavelength bands (Schmit et al. 2017). Radiances reflect atmospheric conditions over a deep layer in clear-sky conditions but are dominated by cloud-top conditions when clouds are present. The ABI radiance observations are available over CONUS at least every 15 min and are converted to brightness temperatures (BTs). The gridded observations used are from channel 10 (7.43-μm lower- to midlevel-tropospheric water vapor channel and a weighting function that peaks near 615 hPa), as assimilated successfully by Zhang et al. (2018, 2019), and are available as the Cloud Moisture Imagery Product (CMIP). Because the *GOES-16* ABI views Earth at an angle, the coordinates of the observations are displaced from their true locations. To account for this, a parallax correction (e.g., Soler and Eisemann 1994; Jones et al. 2020) is applied to the data using its coordinates and the cloud-top height product "ACHA," also from the ABI. The parallax correction varies from roughly 10–20 km, depending on the latitude, longitude, and cloud-top height. The improved position from the parallax correction is important because the parallax error is of the scale of clouds themselves, especially at the time of CI. The BTs are assimilated at their ~2.5-km horizontal resolution. The Community Radiative Transfer Model (CRTM; Han et al. 2006) is the observation operator for simulated BT calculation from WRF-ARW Model output.

The observation height for clear-sky BTs is set to 5000 m, which roughly corresponds to the peak of the weighting function of channel 10 of the ABI. For cloudy-sky conditions, an observation height is found by using cloud-top height product. The designation between clear and cloudy sky is determined by whether there is a value at the corresponding grid point in the cloud-top height product. A vertical covariance localization length of 4.0 of the scale height and a horizontal covariance localization length of 30 km are used, owing to the high density of *GOES-16* observations. Scale height determines the pressure at which the observation will have no influence, using $-\ln(P/P_{\text{ref}})$, where $P_{\text{ref}} = 1000$ hPa and is used to constrain the impact of the observations to that area and to remove the potential for spurious correlations. The observation errors are 2 K for clear-sky radiances and 4 K for cloudy-sky radiances, following Jones et al. (2020), and the BT observations are available at least every 15 min from 1500 UTC 18 May to 0000 UTC 19 May 2018.

2) Clear-air radial velocities from WSR-88Ds

Radial velocities are the component of the velocity of targets toward or away from the radar along a given radar azimuth

angle, which can provide information on the PBL wind field near the radar. Clear-air returns are echoes that are not produced by hydrometeors and typically are present in the PBL out to at least 30 km along all azimuths around the radar site for the lowest several elevation angles with reflectivity values often less than 20 dBZ. Here we use WSR-88D Level-II data from KAMA (Amarillo, Texas), KDDC (Dodge City, Kansas), KFDR (Frederick/Altus Air Force Base, Oklahoma), KFDX (Cannon Air Force Base, New Mexico), KICT (Wichita, Kansas), KTLX (Oklahoma City, Oklahoma), and KVNX (Vance Air Force Base, Oklahoma). The separation of the radars is large enough that regions in between the radars do not have radial velocity observations within the PBL, indicating the impact of the observations is not uniform across the model domain.

Observations with a magnitude less than 2 m s^{-1} or greater than 40 m s^{-1}, or with a distance < 2 km or > 200 km from the radar, or associated with reflectivity ≥ 20 dBZ, are discarded. The remaining velocity data are de-aliased following Eilts and Smith (1990). Superobservations (SOs) with a horizontal spacing of roughly 2 km azimuthally and 10 km radially are created in a manner similar to Zhang et al. (2009) and grouped into spatial bins. This spacing is chosen to best fit the model grid spacing. The standard deviation is calculated for all observations within an elevation and within each bin. If the standard deviation of one bin is greater than 1.5 times the standard deviation of the entire elevation scan, then all observations within the bin are discarded. In each bin, observations that are less than 2 times of the bin's standard deviation from the mean are kept. If more than half of the observations within a bin are discarded during the previous step, then the entire bin is discarded to reduce the influence of noisy observations. Finally, the SO of each bin is designated as the median value of the remaining observations, located in the center of the bin. These SOs are available every 15 min from 1500 UTC 18 May to 0000 UTC 19 May 2018.

The clear-air SO radial velocities have a horizontal localization of 30 km, along with a vertical covariance localization of 0.36 scale height. The radial velocity observation errors are 3 m s^{-1} following Jones et al. (2020). Reflectivity observations are not assimilated.

3) PBL HEIGHT ESTIMATES FROM WSR-88DS

Melnikov et al. (2011, 2013) show that minima in differential radar reflectivity (Z_{DR}) occur at the top of the convective PBL and are caused by Bragg scattering. Banghoff et al. (2018) build on these results to show that quasi-vertical profiles (QVPs; Ryzhkov et al. 2016) of Z_{DR} can be used to identify PBL height. The QVP is created by taking an azimuthal mean of a given radar variable at each range gate, converting radial distance from the radar site to height above ground level (AGL), and then combining successive volume scans to yield a time–height plot of the variable. Banghoff et al. (2018) show that daytime PBL height can be estimated accurately from the height of the temporally coherent minima in Z_{DR} seen in the QVP (Fig. 3).

PBL height observations provide useful information on PBL structure that can be leveraged in CAM data assimilation. PBL heights are calculated at each radar following Banghoff et al. (2018) every 15 min from 1500 UTC 18 May to 0000 UTC 19 May 2018. The PBL height observations are treated as single point observations.

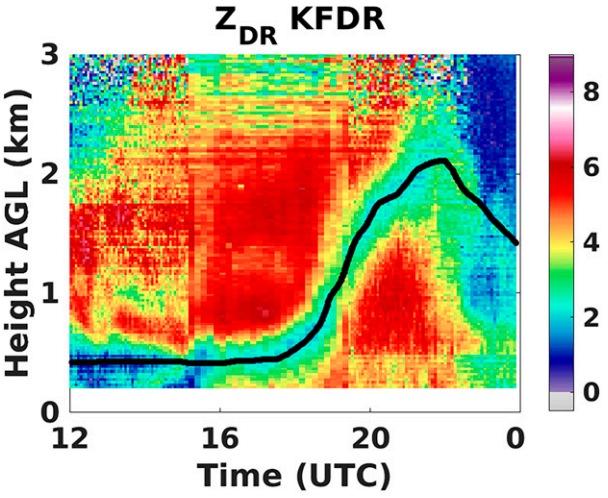

FIG. 3. QVP of Z_{DR} (in dB, shaded according to color bar). Data from the KFDR WSR-88D radar at 4.5° elevation angle from 1200 UTC 18 May to 0000 UTC 19 May 2018. The black line denotes the top of the PBL as estimated from the vertical minimum in Z_{DR}.

The PBL height observation operator is defined as the average value of model diagnosed PBL height over a 10×10 grid point (30 km $\times$ 30 km) region centered on the model grid point closest to the location of the WSR-88D radar corresponding to the PBL height observation. This 900-km^2 region closely approximates the PBL region sampled by the radar in clear-air conditions. Results from single observation tests (not shown) indicate that when a PBL height observation is greater than the background PBL height the increments develop a warmer, deeper and drier boundary layer, whereas when a PBL height observation is lower than the background PBL height the increments develop a cooler, shallower and moister PBL. Based upon the single observation tests and examinations on their correlations with other model state variables, PBL height observations are assimilated using a vertical localization of 2.3 scale height and a horizontal localization of 600 km, as correlations between PBL height and thermodynamic variables are seen to extend above the PBL and over several hundreds of kilometers horizontally (not shown). Based on Banghoff et al. (2018), the observation error for PBL height is set at 250 m.

4) CONVENTIONAL OBSERVATIONS

Standard conventional data from NCEP's Automated Data Processing (ADP) are used in all experiments. The conventional data used includes altimeter setting, temperature, water vapor mixing ratio, pressure, and winds from land stations, radiosonde soundings, and automated aircraft data. The horizontal and vertical covariance localizations are 300 km and 0.4 scale height, respectively. All the covariance localizations are constructed using a fifth-order correlation function, following Gaspari and Cohn (1999). Errors in the conventional data of temperature, moisture, surface pressure, and wind observations are specified

TABLE 1. Observation error, horizontal covariance localization length, and vertical localization length for each observation type.

Observation type	Observation error	Horizontal covariance localization length	Vertical covariance localization length
Conventional	GSI	300 km	0.4 scale height
Clear-air radial velocity	3 m s^{-1}	30 km	0.36 scale height
PBL height	250 m	600 km	2.3 scale height
BT	2 K for clear; 4 K for cloudy	30 km	4.0 scale height

further at http://www.emc.ncep.noaa.gov/mmb/data_processing/prepbufr.doc/table_2.htm. All the errors and covariance localizations for the different types of observations are summarized in Table 1.

d. Experiment design

Four data assimilation experiments are conducted, with all ensemble members run for 3 h, starting at 1200 UTC 18 May 2018, to let errors grow and create flow dependencies. All experiments assimilate data every 15 min from 1500 to 1900 UTC, followed by a 5-h forecast out to 0000 UTC 19 May 2018 free of data assimilation. A control experiment, named "CONV," assimilates conventional observations only and serves as a reference for comparison with the other experiments. Two more experiments assimilate these underused observations from either radar or satellites after conventional observations. "RADAR" has clear-air radial velocities assimilated first, followed by PBL height observations; "SAT" has BT observations assimilated. Last, the "ALL" experiment has all four observation types assimilated: conventional, clear-air radial velocity, PBL height, and BT, in that order. Table 2 summarizes the assimilated observations included in each of the experiments. Figure 4 displays the number of each type of observations during the assimilation period and shows that the numbers of BT and radial velocity SOs are two orders of magnitude more than conventional and PBL height observations. The order in which the observations are assimilated is intended to constrain the large-scale environment first, and then to help define smaller mesoscale and convective features pertinent to CI.

4. Results

a. Validation of increments from assimilated observations

To understand the changes to the analyses from the assimilation of radar and satellite data, three single time data assimilation tests are conducted at 1900 UTC using the background forecasts from CONV. These experiments avoid the problems in interpretation that arise when using different backgrounds and allow one to focus on the contributions of the different observation groups to the analysis. In "RADAR" only clear-air radial velocities and PBL heights are assimilated; in "SAT" only BTs are assimilated; and in "ALL" clear-air radial velocities, PBL heights, and BTs are assimilated.

Results show that the increment patterns are similar in all experiments, but that the larger increments from RADAR extend only from the surface to 700 hPa, while larger increments from SAT and ALL extend throughout the troposphere (Fig. 5). In all three experiments, the increments lead to a warmer and drier PBL to the west of −100.5° and a cooler and moister PBL to the east. A vertical dipole also is seen in which temperature/moisture increments immediately above the PBL between approximately 800 and 700 hPa are opposite in sign to the increments within the PBL. The increments between 800 and 700 hPa often are stronger in RADAR than in SAT. The combination of low-level warming in the PBL and cooling just above the PBL leads to a deeper PBL, whereas low-level cooling in the PBL and warming just above the PBL leads to a shallower PBL. The larger increments just above the PBL in RADAR suggest that the PBL height observation acts to adjust the predicted PBL height to move toward the observation.

Zhang et al. (2022) show that the strongest correlations between BT and model variables in clear-sky conditions occur near the peak of the channel weighting function (~615 hPa for channel 10). The similarities in the low-level increment patterns in Fig. 5 suggest that the increments below 700 hPa are largely produced by the conventional and radar observations. The exception is the large increments west of −102° in SAT and ALL that are associated with observed clouds, whereas the rest of the cross section has clear skies. Horizontal plots of convergence show differences between RADAR and SAT, particularly in the northcentral Texas Panhandle where the wind field in RADAR is convergent in the PBL whereas the wind field in SAT is divergent (not shown). The convergent wind field in RADAR is attributed to the assimilation of clear-air radial velocities owing to its location and shape. Calculations of convective available potential energy (CAPE) indicate that the combination of radar and BT observations leads to a narrowing and strengthening of the zone of highest CAPE in the Texas Panhandle within the region of CI that is weaker in the other experiments (not shown).

TABLE 2. Assimilated observations in each experiment; "Y" denotes that the experiment uses those observations listed above.

Expt name	Conventional	Clear-air radial velocities	PBL heights	BTs
CONV	Y			
RADAR	Y	Y	Y	
SAT	Y			Y
ALL	Y	Y	Y	Y

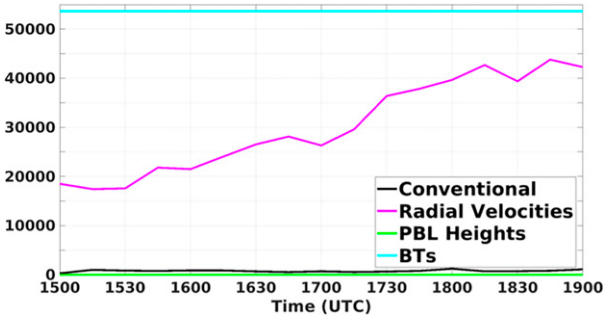

FIG. 4. Number of observations of each type used in the experiments from 1500 to 1900 UTC 18 May 2018. The types include conventional observations (black), clear-air radial velocities (magenta), PBL heights (green), and BTs (cyan).

Results further show that ALL retains many of the features seen in both RADAR and SAT (Figs. 5e,f). The overall assessment is that the radar observations influence the PBL structure and thus can yield an improved analysis of the preconvective low-level environment, while the BT observations yield an improved analysis of ongoing convection and the atmospheric state above the capping inversion. It is encouraging that adjustments from both radar and satellite data assimilation are maintained when they are simultaneously assimilated.

b. *Assimilation and forecast period verification*

To assess the impact of assimilating PBL heights, clear-air radial velocities, and BTs using the EnKF during the assimilation window and the subsequent ensemble forecasts, the observation-space diagnostic metric of bias-corrected root-mean-square innovation/error (hereafter RMSI/RMSE) is used. RMSIs are calculated from 1500 to 1900 UTC, and RMSEs are calculated from 1900 UTC 18 May to 0000 UTC 19 May 2018. RMSI (RMSE) is defined as

$$\text{RMSI} = \sqrt{\langle (\mathbf{d} - \overline{\mathbf{d}})^2 \rangle},$$

where $\mathbf{d} = \mathbf{y}^o - H(\overline{\mathbf{x}^b})$ is the innovation (error) of the background (forecast) ensemble mean, and $\mathbf{y}^o$ represents the observations.

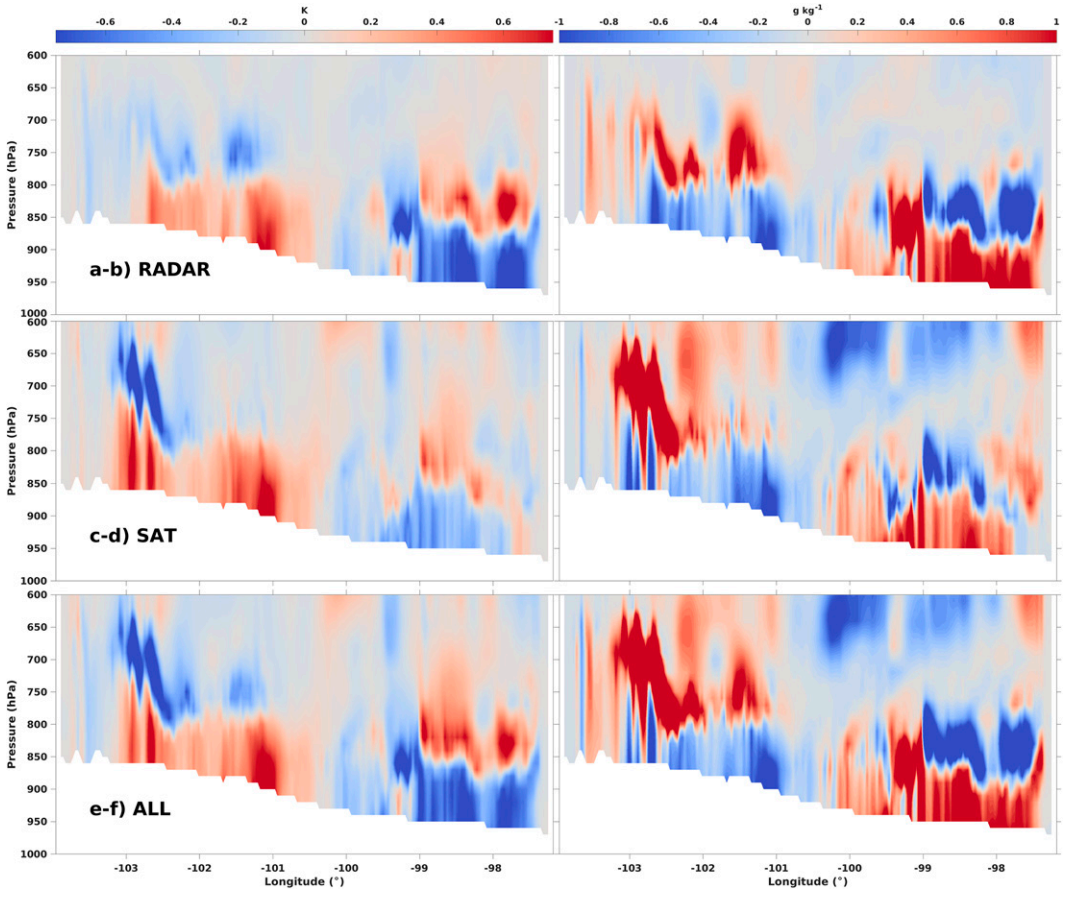

FIG. 5. West-to-east vertical cross sections along 35°N of (a),(c),(e) ensemble-mean increments (posterior minus prior) of potential temperature (in K) and (b),(d),(f) water vapor mixing ratio (in g kg^{-1}) in the (a),(b) RADAR; (c),(d) SAT; and (e),(f) ALL single-time data assimilation tests. Note that horizontal plots show that these patterns extend horizontally as well as vertically. Potential temperature increments vary from −0.8 to 0.8 K and water vapor mixing ratio increments vary from −1 to 1 g kg^{-1}.

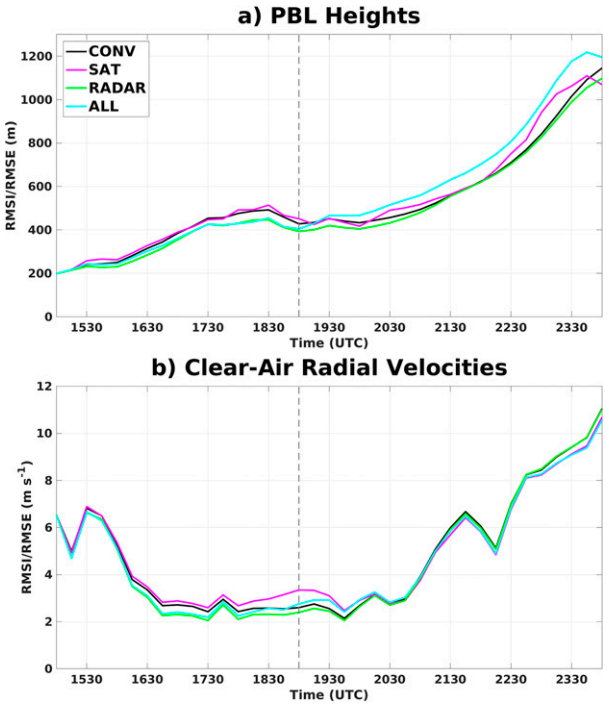

FIG. 6. Values of RMSI and RMSE vs time (UTC) for (a) PBL heights (m) and (b) clear-air radial velocities (m s^{-1}) from 1500 UTC 18 May to 0000 UTC 19 May 2018 from the following experiments: CONV (black), RADAR (green), SAT (magenta), and ALL (cyan). Vertical line (dashed gray) at 1900 UTC indicates the transition from the assimilation period to the forecast period.

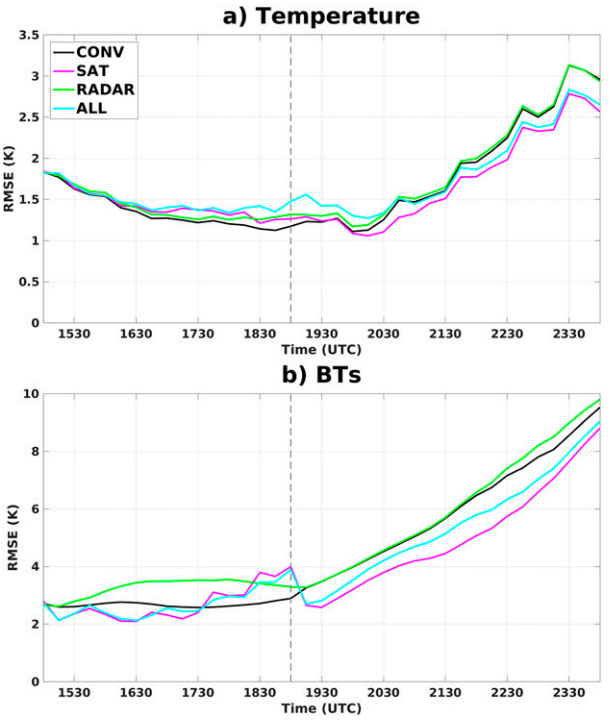

FIG. 7. Values of RMSE vs time (UTC) for (a) 2-m air temperature (K) and (b) channel-8 BTs (K) from 1500 UTC 18 May to 0000 UTC 19 May 2018 for the following experiments: CONV (black), SAT (magenta), RADAR (green), and ALL (cyan). Vertical line (dashed gray) at 1900 UTC indicates the transition from the assimilation period to the forecast period.

Innovations are only valid for times or variables where the observations are directly assimilated. The square of differences of each innovation from the domain average of all innovations $\overline{\mathbf{d}}$ is calculated as the average value in brackets. H is the observation operator during the assimilation period or forecast model, which is the PBL height operator, the radar radial velocity operator, or the CRTM for BTs. $\mathbf{x}$ is the model state vector with superscript b denoting the background ensemble-mean forecasts. Smaller RMSI (RMSE) values indicate smaller discrepancies from the observations and hence better analysis and forecast accuracy.

The evolution of RMSIs for PBL heights and clear-air radial velocities during the assimilation period (1500–1900 UTC) and RMSEs during the forecast period (1900–0000 UTC) for the assimilated variables for all four experiments is shown in Fig. 6. For PBL height (Fig. 6a), all experiments begin with RMSIs close to 200 m and increase approximately linearly with time over the next 3 h. A bifurcation occurs around 1730 UTC between the experiments that do and do not assimilate PBL heights, with CONV and SAT having larger RMSIs than experiments that assimilate PBL heights (RADAR and ALL). This bifurcation occurs as the PBL begins to deepen more rapidly (e.g., Fig. 3) after the morning stable layer is removed by surface heating. By 1900 UTC, RADAR has the lowest RMSI value (near 400 m), whereas SAT has the largest RMSI value (near 450 m). It is encouraging that the PBL height assimilation improves PBL analyses with respect to observed values, even though the land surface variables are not updated during assimilation. During the forecast period from 1900 to 0000 UTC, the RMSEs increase in all four experiments as the PBL deepens, with RADAR having the lowest RMSE over the forecast period. Most experiments have RMSEs near 600 m at 2200 UTC, with values nearly doubling by 0000 UTC. The experiments that assimilate BTs all have larger RMSEs at the end of the forecast period compared to the experiments that do not assimilate BT, suggesting that the assimilation of BT observations can negatively influence PBL height forecasts. However, as is shown later, the experiments that assimilate BTs also develop more convection; it may be the impact of convection on the PBL that produces these differences.

In contrast to PBL heights, RMSIs for clear-air radial velocities decrease over the first few cycles of assimilation, approaching values near 2 m s^{-1} by 1700 UTC (Fig. 6b). These values are of similar magnitude to those seen when assimilating radial velocity observations in precipitation (Yussouf et al. 2013). SAT has the largest RMSI, whereas RADAR has the smallest RMSI by 1900 UTC. It is encouraging that the two radar observations work synergistically in RADAR to yield an improved analysis of the PBL wind field. As seen with PBL heights, clear-air radial velocities see a notable increase in RMSEs during the forecast period. However, unlike PBL height assimilation, there is no clear difference in RMSEs between the four experiments

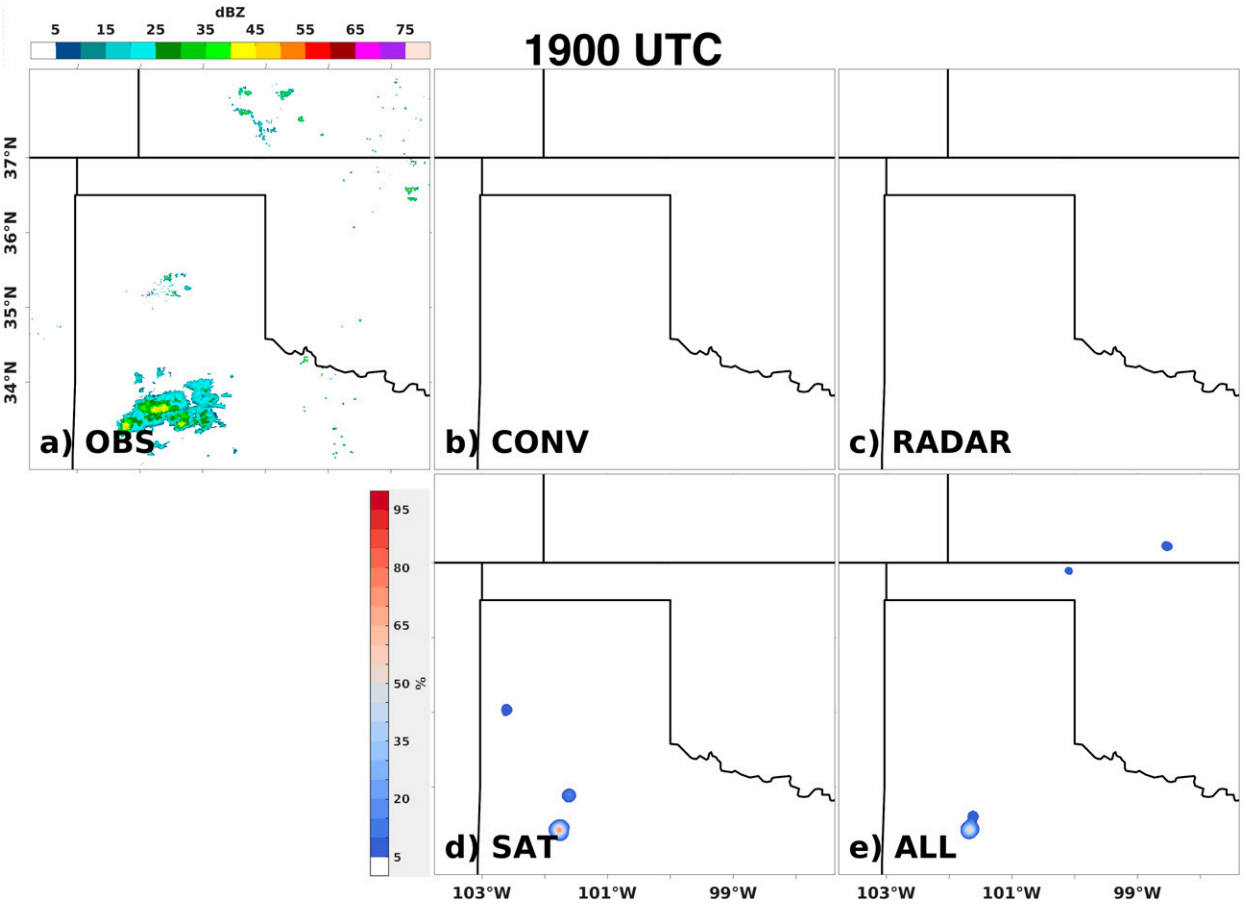

FIG. 8. (a) Observed composite reflectivity and neighborhood ensemble probability of simulated composite reflectivity exceeding 35 dB*Z* for the (d) CONV, (c) RADAR, (d) SAT, and (e) ALL experiments at 1900 UTC 18 May 2018.

after 2000 UTC, suggesting that the improvements in the PBL wind field from clear-air radial velocity assimilation have a short lifetime.

Two different sets of observations not used in assimilation, *GOES-16* ABI channel-8 infrared BTs and 2-m air temperatures from state-run mesonets, are used for verification (Fig. 7). Observations from both the Oklahoma (Brock et al. 1995; McPherson et al. 2007) and West Texas (Schroeder et al. 2005) Mesonets, which are not assimilated in any of the experiments, are used to calculate RMSEs of 2-m air temperature every 15 min from 1500 to 0000 UTC. RMSEs calculated from the Mesonet observations are near 1.8 K to begin, and steadily improve throughout the assimilation period (Fig. 7a). By 1900 UTC, RMSEs of CONV are near 1.15 K and the lowest of all four experiments. Curiously, ALL surprisingly has the highest RMSEs by the end of the assimilation period, although the differences are not large. Reasons for this behavior are unclear, although the impacts of spurious convection (shown later) may play a role. In contrast, during the forecast period the experiments that assimilate BT observations have smaller RMSEs than those without. At 0000 UTC, RMSEs from CONV and RADAR are at 3 K, while SAT and ALL are closer to 2.5 K. Verification of 2-m dewpoint temperature yields similar results, but with less differentiation between experiments (not shown).

RMSEs of BTs from all experiments are identical at 1500 UTC, with values near 2.8 K (Fig. 7b). However, after one assimilation cycle, the experiments assimilating BTs (SAT and ALL) have RMSEs slightly lower than the experiments that do not assimilate BTs (CONV and RADAR). Although the RMSEs of SAT and ALL are initially lower than RADAR and CONV, SAT and ALL are higher by 1900 UTC, which is likely related to spurious convection. Early in the forecast period, experiments with channel-10 BTs assimilated see a noticeable decrease in RMSEs for channel-8 BTs. SAT and ALL have comparable RMSEs, but all experiments see an increase in RMSE from 3 to 4 K at 1900 UTC to nearly 10 K at 0000 UTC in the poorest performing experiments, CONV and RADAR.

The RMSIs and RMSEs suggest that during the assimilation and forecast periods the PBL height and BT observations produce longer-lasting positive impacts on the ensemble forecasts. In contrast, the assimilation of clear-air radial velocity improves RMSEs for roughly an hour after the end of the assimilation period. It is encouraging that the independent observations of 2-m air temperature show the ensembles with BT assimilation are more accurate than the ensembles without BT assimilation.

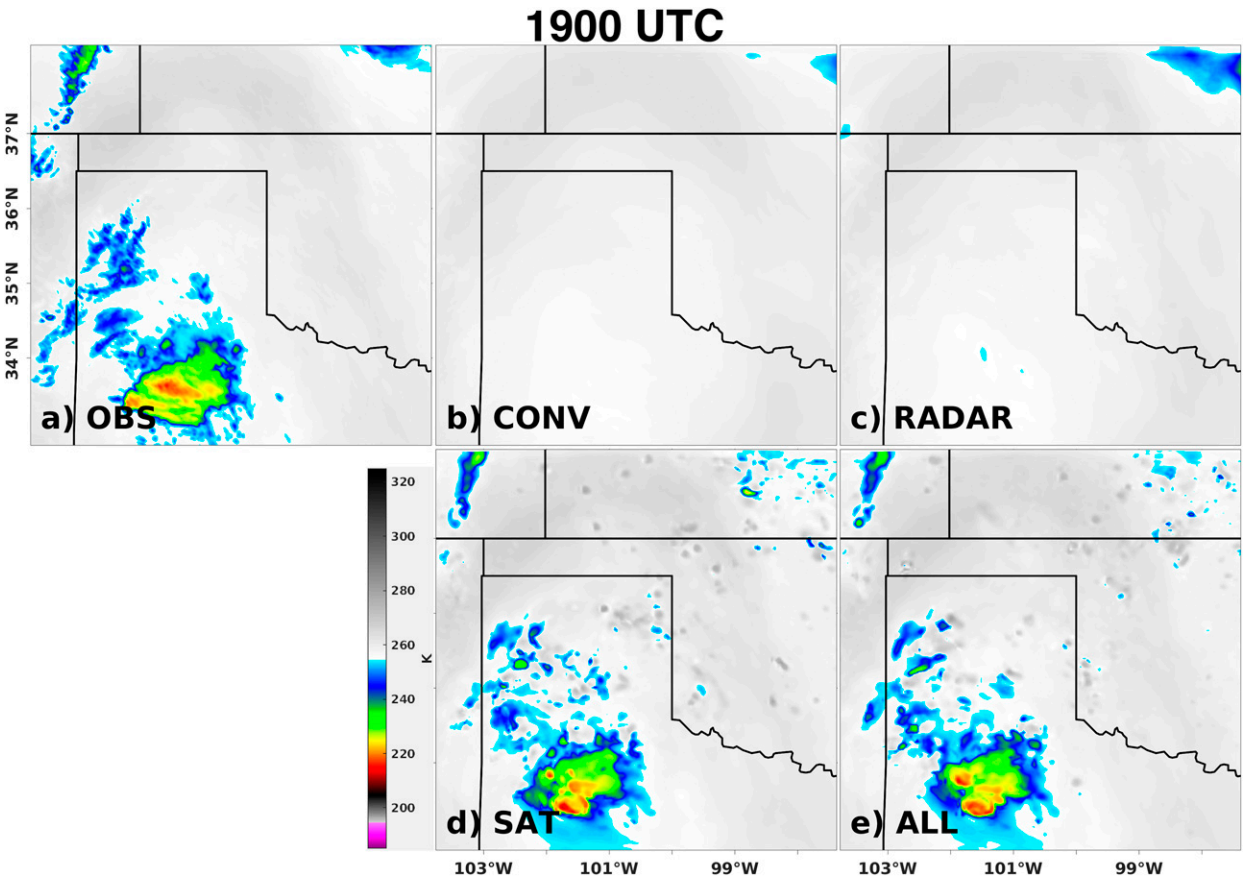

FIG. 9. (a) Observed brightness temperature of channel-10 *GOES-16* ABI and ensemble-mean CRTM simulated ABI channel-10 BTs for the (b) CONV, (c) RADAR, (d) SAT, and (e) ALL experiments at 1900 UTC 18 May 2018.

Differences between experiments that did and did not assimilate radar data are minimal, as seen when comparing CONV to RADAR and SAT to ALL.

c. *Convection initiation*

A qualitative evaluation of the experiments furthers an understanding of the potential value of assimilating BT observations, clear-air radial velocities, and PBL height for CI forecasts. Neighborhood ensemble probabilities (NEPs) of simulated composite reflectivity (Schwartz and Sobash 2017) exceeding 35 dBZ for the experiments display several characteristic behaviors at the end of the assimilation period at 1900 UTC (Fig. 8). A 9-km-radius circle for the neighborhood is used to account for the horizontal displacements of convection that can occur within individual ensemble members. First, the experiments without BT assimilation (CONV and RADAR) fail to develop convection anywhere in the model domain by the end of the assimilation period. As shown later, this lack of deep convective activity persists for several hours and limits the accuracy of the CI forecasts. Second, the experiments that assimilate BT (SAT and ALL) capture the ongoing convection in the southern Texas Panhandle to various degrees, with NEPs above 90%, but also produce scattered storms in other parts of the domain. The benefit of satellite data is even more clearly shown when the ensemble mean BTs are compared against observations (Fig. 9). Only experiments with BTs assimilated have clouds with temperatures below 265 K (SAT and ALL). However, scattered convective cells develop in one or two ensemble members as seen by the speckled pattern in the simulated BTs, with SAT appearing to have more spurious storms than ALL.

The deep convection that initiates in the northeastern Texas Panhandle at 2130 UTC has developed into several isolated storms with reflectivity values $>$ 55 dBZ by 2200 UTC (Fig. 10a). Also, the observed region of deep convection in the southern Texas Panhandle has increased in intensity and coverage over the past few hours and is seen in the corner of the smaller domain. The experiments without BTs assimilated produce deep convection in only a few ensemble members in the southern Texas Panhandle where no convection is observed (Figs. 10b,c). In contrast, SAT and ALL develop deep convection in the northeastern Texas Panhandle (Figs. 10d,e), although the NEPs for SAT are low. In contrast, ALL has NEPs above 20% in the vicinity of observed CI. These comparisons suggest that the combined radar and satellite observations assimilated in ALL help place CI in roughly the correct location and time 3 h after the data assimilation cycling ends. This is ultimately due to improved PBL, dryline

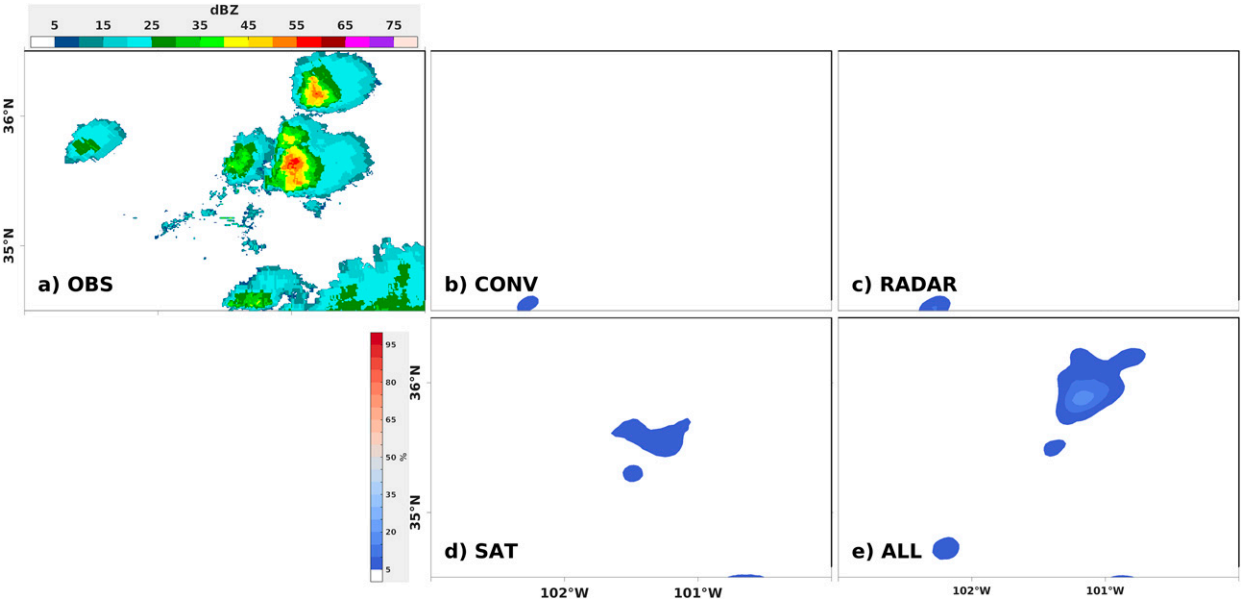

FIG. 10. (a) Observed composite reflectivity zoomed into the Texas Panhandle region and zoomed-in neighborhood ensemble probability of simulated composite reflectivity exceeding 35 dBZ for the (b) CONV, (c) RADAR, (d) SAT, and (e) ALL experiments at 2200 UTC 18 May 2018.

and cold pool representation on this case day from radar and satellite data.

The observed BTs at 2200 UTC (Fig. 11a) show several small regions of colder (and taller) cloud tops in the northern Texas Panhandle where the CI of interest occurred, indicating the location of the most intense convection. Ensemble means of simulated BTs in CONV and RADAR (Figs. 11b,c) still lack any cold cloud tops (below ~230 K) outside of Colorado. SAT and ALL show colder cloud tops from earlier convection in the southern Texas Panhandle (Figs. 11d,e), and indicate the formation of colder cloud tops, synchronous with observations, in the northern Texas Panhandle. ALL appears to have some of the coldest cloud tops compared to observations, with some spurious convection in southern Kansas. The spurious convection in Kansas occurs in all experiments, but is more widespread in the ensembles that assimilate BT.

At the end of the forecast period at 0000 UTC, all the experiments without BTs assimilated continue to underpredict the observed convection (Fig. 12). Some members produce a line of convection that stretches northeastward from a point in the Oklahoma Panhandle region into Kansas, perhaps best seen in RADAR (Fig. 12c). The ensemble-mean simulated BTs from SAT and ALL better agree with the observed BTs in terms of the location of the coldest cloud tops, although with a noticeable eastward shift in the overall convective region.

Another observation that is not directly assimilated is radar reflectivity, which is used to quantitatively compare the ensemble forecasts. Ensemble equitable threat scores (ETS; Wilks 2011) are selected to examine the simulated composite reflectivity forecasts during both the assimilation window and the forecast periods. Positive values relative to CONV are considered success in that there is improvement in the prediction of deep convection. These values can vary greatly from experiment to experiment, as the ETS is sensitive to location displacement errors. The domain used for these calculations is shown in Fig. 2a and centers on the Texas Panhandle where CI is observed. ETS is defined as

$$\mathrm{ETS} = \frac{H - R}{H + M + F - R},$$

where

$$R = \frac{(H + M)(H + F)}{n},$$

H, M, and F are the number of total hits, misses, and false alarms, respectively, calculated from all 40 ensemble members, and n is the total number of grid points that are used for the calculation. ETS values above 0 indicate skill compared to a random forecast, with skill improving as values approach 1. Because reflectivity is not assimilated, and the convective regions of interest are not present at the end of the data assimilation period, the expectation is that ETS values will be positive, but well below 0.5. To account for small, horizontal displacements in individual ensemble members, a neighborhood maximum (NM) approach is used (Schwartz 2017) for the ETS calculation. An event occurrence is determined by whether an event occurs *anywhere* within the neighborhood (defined as a 9-km-radius circle) of the forecast or observation point. Hits are designated when the forecast and observed event occurs in the neighborhood, while false alarms occur when a forecast event happens, but no observed event occurs in the neighborhood. For misses, this is designated when the

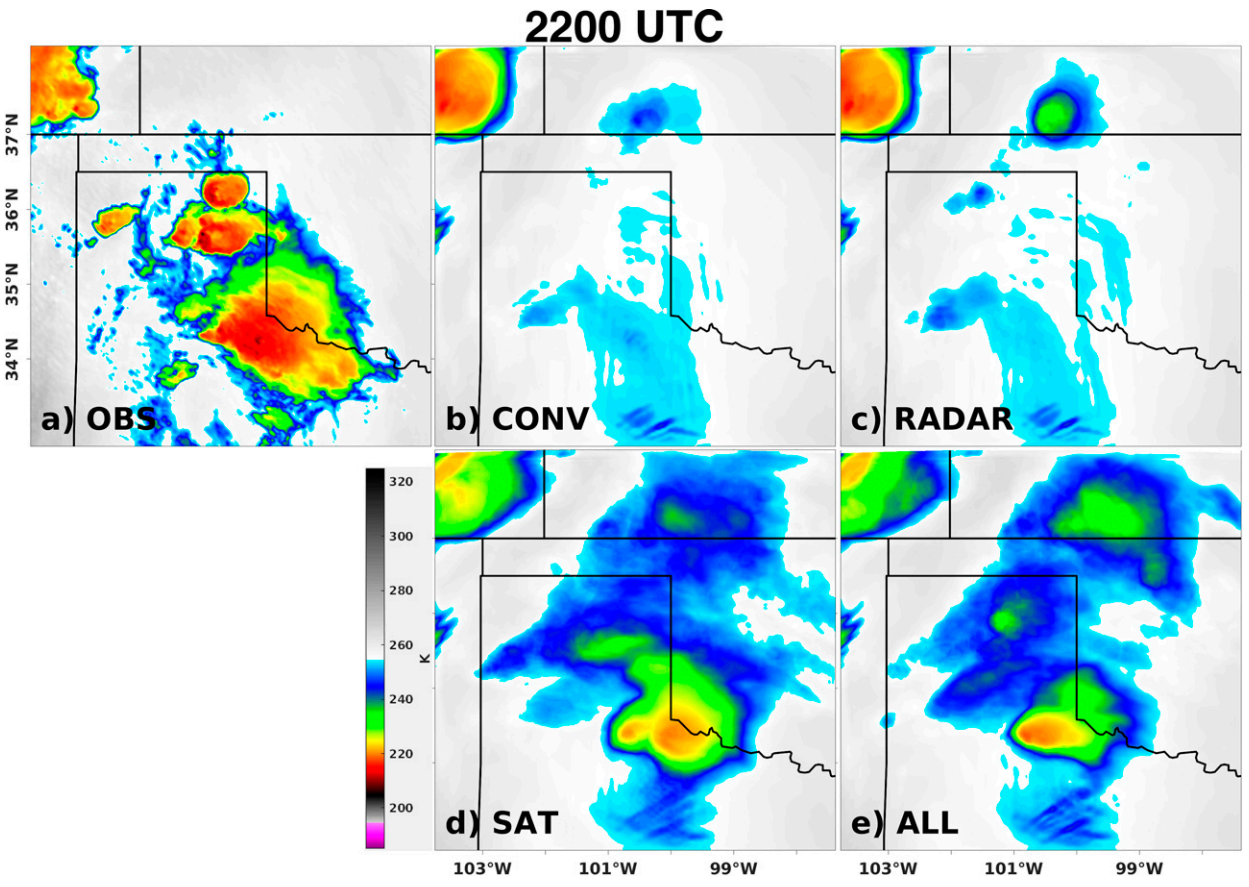

FIG. 11. (a) Observed brightness temperature of channel-10 *GOES-16* ABI and ensemble-mean CRTM simulated ABI channel-10 BTs for the (b) CONV, (c) RADAR, (d) SAT, and (e) ALL experiments at 2200 UTC 18 May 2018.

observed event occurs in the neighborhood, but the forecast does not. Vertical displacements in individual ensemble members are not accounted for in the analysis.

The reflectivity observations are from the Iowa Environmental Mesonet radar mosaic archive (https://mesonet.agron.iastate.edu/). Simulated reflectivity is first interpolated to the radar's lowest elevation scan (i.e., base reflectivity), and then a composite of base reflectivity is taken from the lowest elevation scan. Like the radial velocities, reflectivity observations are dense, so thinning is used for comparison between the observed values and the model output. For each of the radars, thinning is employed such that the horizontal grid spacing is approximately 3 km. Therefore, n is the number of reflectivity observations at each evaluation time multiplied by the number of ensemble members (40). Reflectivity thresholds of 20 and 35 dBZ are used in the calculations, with 20 dBZ chosen to represent regions of general precipitation, and 35 dBZ is chosen to represent regions of convective precipitation.

Values of NM ETS for the 20-dBZ threshold are close to 0 early on when there is no significant precipitation or organized convection in the model subdomain, as expected (Fig. 13a). The NM ETS values that are slightly above zero prior to 2100 UTC are produced by ground clutter overlapping with a weak cell in a few ensemble members. Only after CI around 2115 UTC do NM ETS values from the experiments containing satellite observations increase. The experiments that assimilate BTs see an increase in NM ETS values, with SAT and ALL having the largest increase in NM ETS between 2100 and 2230 UTC, as the areal coverage of convection increases. By 0000 UTC, ALL has the largest NM ETS of the experiments. Values of NM ETSs for CONV and RADAR increase only after 2200 UTC, reaching only ~0.12 toward the end of the forecast. Although the experiments that did not assimilate satellite data struggled with CI, the location of observed storms align with these experiments ~2 h later. Focusing on the time near CI (roughly 2100–2230 UTC), the experiments with satellite data assimilation have the largest values of NM ETS, showing their ability to capture the CI and its early evolution.

Figure 12b displays NM ETSs using the 35-dBZ threshold. SAT and ALL again have the largest NM ETSs throughout the forecast period, getting close to 0.1 by 0000 UTC. Similar to the 20-dBZ threshold (Fig. 13a), values of NM ETS in SAT and ALL increase sharply around 2100 UTC, close to when observed CI occurs. Experiments that did not assimilate BTs only begin to show an increase in NM ETS after 2200 UTC. Differences are relatively minor when directly comparing ALL and SAT or RADAR and CONV, but the experiments

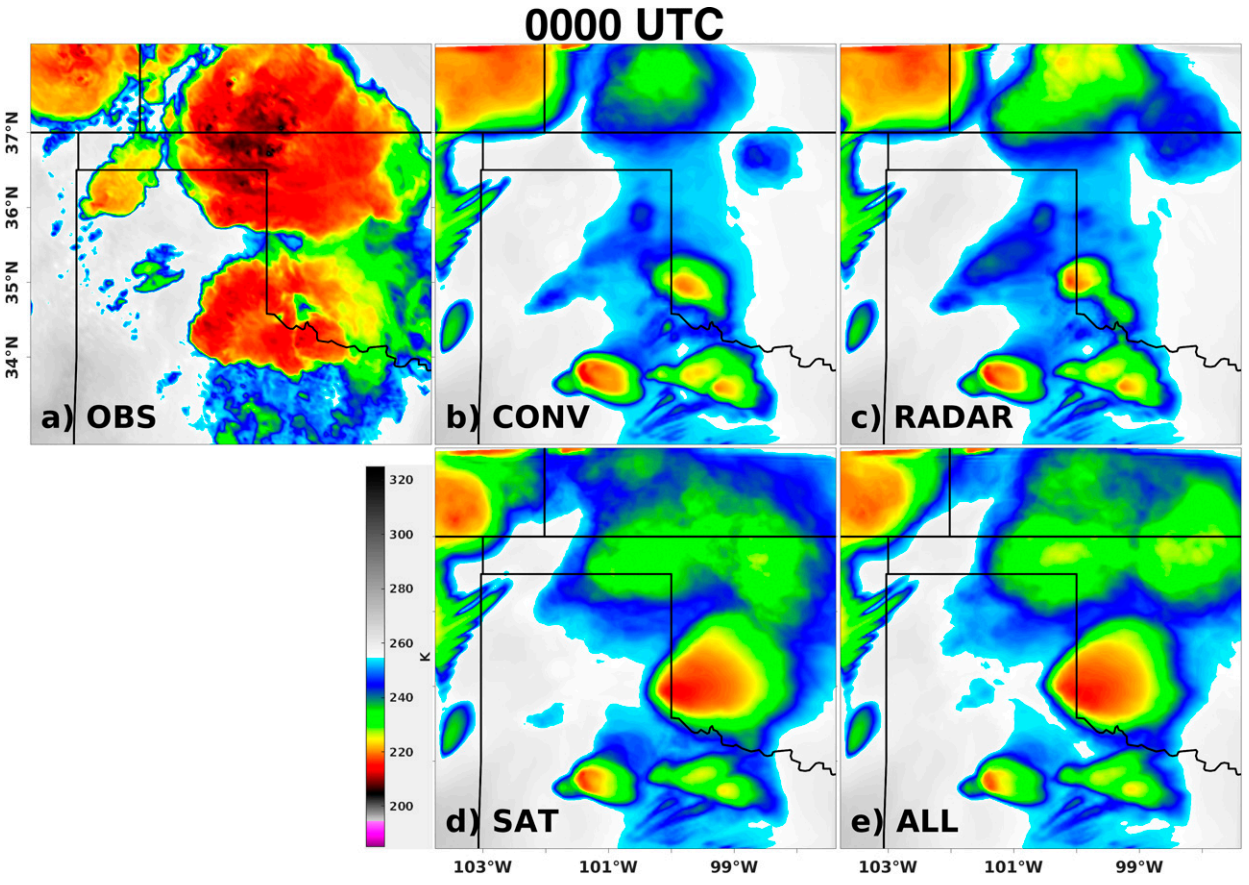

FIG. 12. (a) Observed brightness temperature of channel-10 *GOES-16* ABI and ensemble-mean CRTM simulated ABI channel-10 BTs for the (b) CONV, (c) RADAR, (d) SAT, and (e) ALL experiments at 0000 UTC 19 May 2018.

in those pairs that assimilate satellite data, ALL and SAT, again have slightly larger NM ETS values from the time of CI until the end of the free forecasts for this larger reflectivity threshold.

d. Features leading to CI

A careful subjective evaluation of each of the 160 ensemble forecasts is conducted to determine the model features that lead to CI. Selected model fields are animated and evaluated over the 2-h period prior to CI. This analysis shows that there are two primary mesoscale features present in individual members that ultimately lead to CI: 1) the dryline, and 2) outflow boundaries from convection that initiates in the southern portion of the domain around 1830 UTC during the data assimilation window.

To quantify the influence that the dryline and outflow boundaries have on CI occurrence, identification of these features at the time of initial CI is done for each individual

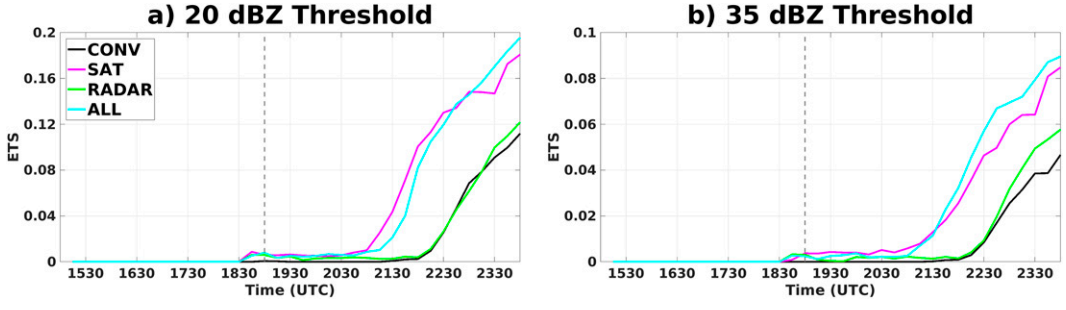

FIG. 13. Values of neighborhood maximum ETS vs time (UTC) for composite radar reflectivity using (a) a 20-dB*Z* threshold and (b) a 40-dB*Z* threshold, from 1515 UTC 18 May to 0000 UTC 19 May 2018, for the following experiments: CONV (black), RADAR (green), SAT (magenta), and ALL (cyan).

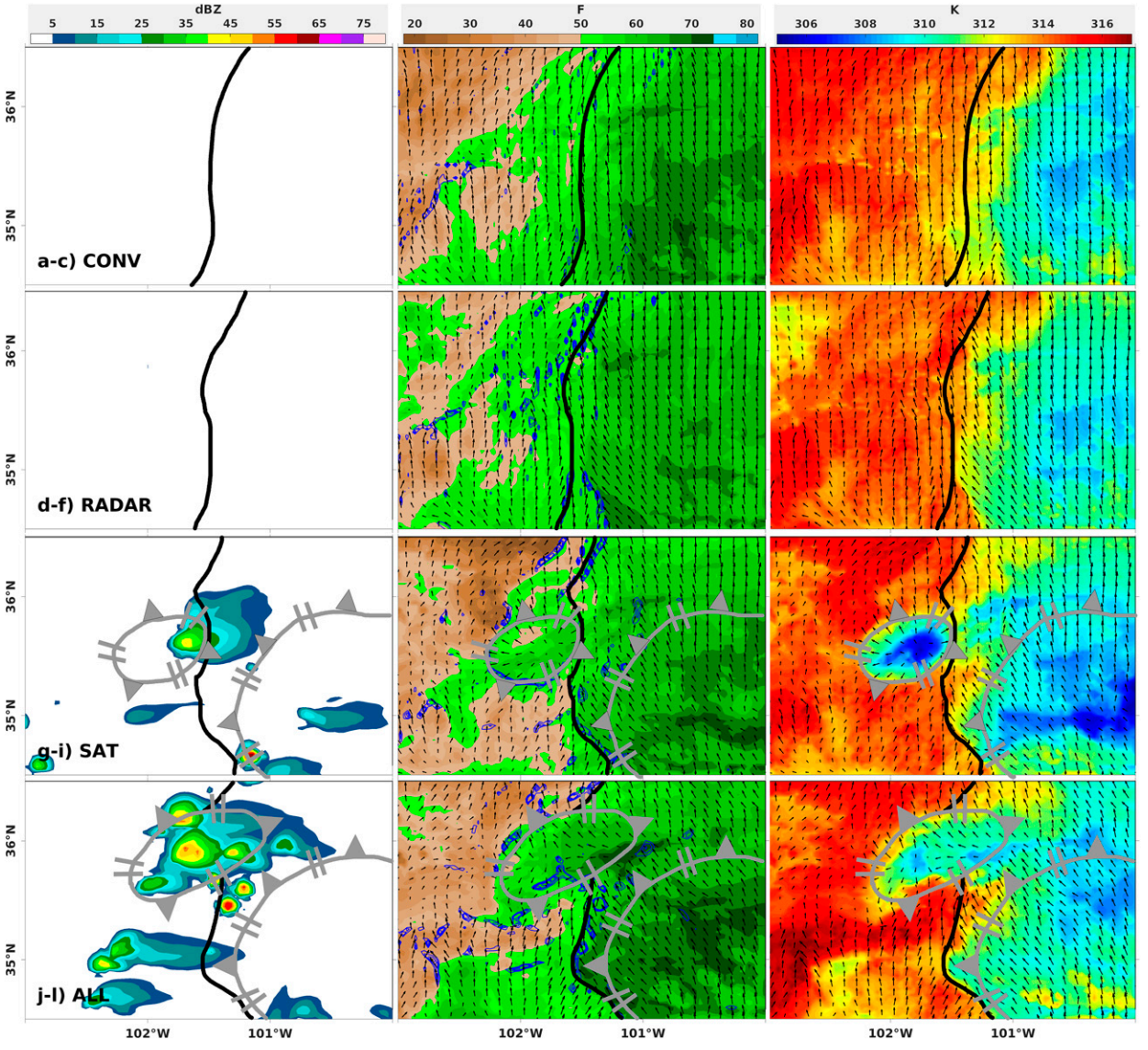

FIG. 14. (a),(d),(g),(j) Simulated composite reflectivity; (b),(e),(h),(k) surface dewpoint temperature (shaded), maximum vertical velocity between the surface and 800 hPa (blue), and wind vectors; and (c),(f),(i),(l) surface potential temperature (shaded) and wind vectors for (a)–(c) ensemble member 11 of CONV, (d)–(f) ensemble member 24 of RADAR, (g)–(i) ensemble member 40 of SAT, and (j)–(l) ensemble member 20 of ALL experiments at 2100 UTC 18 May 2018. The range of contours for maximum vertical velocity is 0.75 m s^{-1}, by increments of 0.25–1.5 m s^{-1}. The dryline (black line) and outflow boundaries (gray line) are annotated.

ensemble member in the experiments. The process begins by first determining if CI occurs between 1900 and 2130 UTC anywhere in the subdomain that covers the Texas Panhandle (Fig. 2a). Composite reflectivity values greater than 10 dB*Z* at any point in this domain constitute CI, even if the convection does not persist.

Identification of the dryline and outflow boundaries in the model forecasts is done through a subjective analysis of lowest model level potential temperature, mixing ratio, and wind vectors, and maximum vertical velocity between the surface and 800 hPa (i.e., within the PBL). An example of these variables at 2100 UTC is shown in Fig. 14 for a selected ensemble member from each of the experiments. The analysis indicates that ensemble member 11 in CONV and member 24 in RADAR have no CI at this time, ensemble member 40 in SAT has CI associated with the dryline, and ensemble member 40 in ALL has CI associated with both the dryline and outflow boundaries. Individual members are chosen to be representative cases showing the features for the corresponding experiment.

Results from all members indicate that CONV and RADAR do not exhibit CI from outflow boundaries in any of their 40 members prior to the initial CI event, as they do not capture the ongoing convection in the southern portion of the model

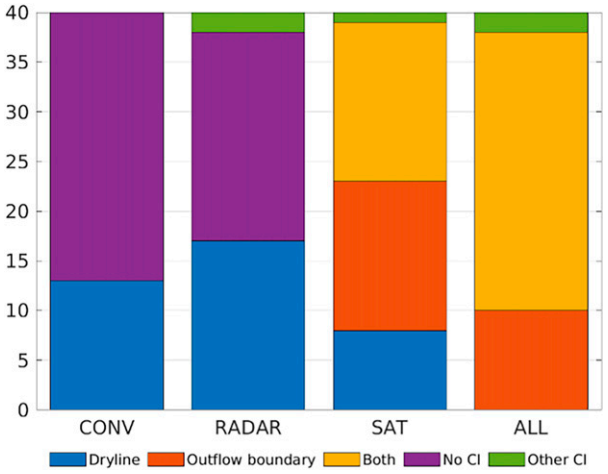

FIG. 15. Bar graph of model features associated with CI in individual ensemble forecasts in the CONV, RADAR, SAT, and ALL experiments. CI via the dryline (blue), outflow boundary (orange), both features (yellow), no CI (purple), and CI occurring that did not meet the criteria in section 4c (green) are shown.

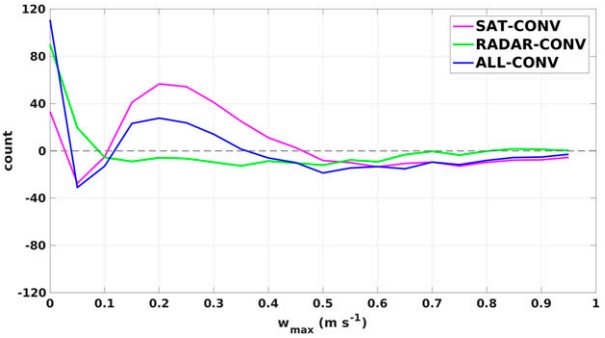

FIG. 16. Histogram showing differences in counts of maximum PBL vertical motion between CONV and the other three experiments at 2100 UTC 18 May 2018: RADAR-CONV, SAT-CONV, and ALL-CONV. Histogram bins are every 0.05 m s^{-1}.

domain (e.g., Figs. 9b,c). However, in both SAT and ALL the earlier convection that starts near 1830 UTC 19 May 2018 to the south produces outflow boundaries beginning around 1930 UTC that generally travel northward and are present in many members. We use the following criteria to quantify the overall frequency that the mesoscale features are associated with CI; if the dryline or outflow boundary is within five model grid points (15 km) of CI, that feature is associated with CI for the ensemble member. If both the dryline and outflow boundary are within 5 model grid points of CI, then both features are associated with CI for the ensemble member.

Figure 15 shows a bar graph of the number of ensemble members (out of 40) that have CI associated with the either the dryline, outflow boundary, both, no CI, as well as members that have CI but did not meet the distance criterion for the dryline or outflow boundary. Results show that CONV has roughly one-third of its members (13 of 40) producing CI, which occurs exclusively in association with the dryline. Most members in CONV do not forecast CI, however, and when they do forecast it, the resulting convection is often short-lived. Results for RADAR show that CI is produced 46% more often than in CONV (19 of 40 in RADAR), suggesting again that the radar observations are adding value to the ensemble. Both CONV and RADAR, lacking BT assimilation, do not capture the earlier convection to the south, which negatively influences their ability to produce CI.

In contrast to CONV and RADAR, SAT and ALL both have 40 members producing CI. SAT has 8 members that produce CI exclusively associated with the dryline, while no members from ALL are only linked to the dryline. Most ensemble members in SAT have CI associated outflow boundaries (31 of 40), with 15 of these members producing CI exclusively associated with an outflow boundary, more than any other experiment. In ALL, most members have both the dryline and outflow boundaries present near CI (28 of 40), which is significantly more than in SAT (16 of 40). Based on Fig. 15, radar data improves characterization of the dryline, while satellite data improves representation of ongoing convection, which leads to cold pools that help trigger CI hours later.

One reason why the experiments that assimilate BT observations are more successful in producing CI is likely related to their prediction of lift. Histograms are produced of the maximum PBL (i.e., surface to 800 hPa) vertical motion at each grid point in the smaller domain, with bins every 0.05 m s^{-1}. To highlight differences from CONV, the histogram counts from CONV are subtracted from the histogram counts for RADAR, SAT, and ALL and plotted. Results from 2100 UTC (Fig. 16) show that SAT and ALL have more grid points with maximum vertical motion between 0.2 and 0.4 m s^{-1}, values typically associated with mesoscale features such as a dryline or outflow boundary in the model (larger values are typically associated with deep convection). Lock and Houston (2014) investigate forecasts from the 20-km Rapid Update Cycle (RUC) model and conclude that the amount of predicted lift often separates CI and no-CI events. Thus, our results suggest that the assimilation of BT observations leads to stronger lift in the forecasts, which is associated with the dryline and outflow boundaries. Results from RADAR are unclear, as it produces weaker vertical motions than CONV, but circumstantial evidence suggests that the areas of vertical motion in RADAR are more coherent than found in CONV (see Fig. 14) and may be more favorable for the sustained lift needed for CI. Similarly, it is also unclear why ALL has weaker vertical motions than SAT, although fewer spurious storms may be a contributing factor (see Fig. 9).

5. Summary

A case study is used to explore whether the assimilation of *GOES-16* BT observations and underutilized WSR-88D observations of PBL height and clear-air radial velocities combined can yield improvements to CAM ensemble forecasts of CI on 18 May 2018. The GSI EnKF is used to assimilate the observations over a 4-h window from 1500 to 1900 UTC into

40-member ensembles. All experiments assimilate conventional observations, with additional experiments produced with and without the radar and BT observations assimilated and results compared with observations. Ensemble forecasts for all 4 experiments are valid from 1900 UTC 18 May to 0000 UTC 19 May 2018. Results show that ALL, the experiment that assimilates conventional, radar and satellite data, yields improved 2.5-h forecasts of CI in the Texas Panhandle compared to the other experiments. The experiments without BT assimilation, CONV and RADAR, are unable to develop convection at the right time and place.

Both the radar and satellite data appear to provide unique benefits during the assimilation period. The RMSI and RMSE calculations suggest that the assimilation of PBL height and BTs produce a longer-lasting positive impact on the ensemble forecasts than seen with the assimilation of clear-air radial velocity. Surface 2-m air temperature RMSEs are lower in experiments that assimilate BTs, suggesting that improvements to the cloud field analyses can also improve low-level temperatures. Results from a feature-driven subjective analysis show that outflow boundaries moving northward from deep convection to the south are key to producing CI in many of the ensemble members, as these boundaries produce the stronger lift needed for CI. Although channel-10 BTs are sensitive to middle atmosphere water vapor, changes to the analyses from satellite data also are seen in temperature. The results highlight the value of representing ongoing convection in model initial conditions, because without this information, the subsequent predictions of deep convection are less accurate. Results suggest that while BT assimilation alone is valuable, the ensembles with satellite DA further improve when the WSR-88D radar observations of PBL height and clear-air radial velocity are assimilated, which alter the PBL structure in the analyses and lead to better 2-m temperature forecasts within the preconvective environment. Radar data assimilation alone yields increases in the probability of CI in the Texas Panhandle, but not in a particular location. The radar observations are most valuable when they are assimilated concurrently with satellite data. Another concern in the ensemble forecasts is the prevalence of widespread, scattered, spurious convection resulting from the BT assimilation, deserving further attention.

The CAM ensemble results suggest that there is promise for improved forecasts of CI timing and location, several hours out from initialization, via the assimilation of clear-air radar and satellite observations linked to moisture, instability, and lift – the three ingredients of CI. The observations of PBL height, clear-air radial winds, and BTs appear to work synergistically to provide improved initial conditions for the ensemble forecasts. Although these results are from a single case study, they are suggestive of the potential value of these new observations. Future studies are needed to determine whether the assimilation of radar and satellite observations for the depiction of the PBL and cloud field can consistently improve the prediction of severe weather. Future studies also should explore how other routine observations that are available can be leveraged in CAMs for accurate CI predictions. Additionally, an unexplored question in this work is the impact of the order of assimilation for the observation types on the final analyses. Sensitivities to the order are not explored in this paper, but warrants consideration, particularly with underused observation types such that they can be used optimally to improve analyses and forecasts in concert with observations that are already assimilated.

Acknowledgments. The authors thank Professor Xuguang Wang and Mr. Sam Degelia from the University of Oklahoma for support and guidance with configuring the GSI-EnKF to ingest new observation types. The authors also thank numerous scientists at the Global Systems Division (GSD), Environmental Modeling Center (EMC), and National Severe Storms Laboratory (NSSL) of NOAA for their assistance with GSI and helpful discussions. The authors also thank three reviewers for their valuable feedback and suggestions. This work was supported by NOAA Grant NA18OAR4590369, as well as the Future Investigators in NASA Earth and Space Science Technology (FINESST) Grant 80NSSC20K1619. The findings and conclusions presented do not necessarily reflect the view of the funding agencies NOAA or NASA. Data assimilation and numerical simulations were performed on the Stampede 2 supercomputer of the Texas Advanced Computing Center (TACC) under the Extreme Science and Engineering Discovery Environment (XSEDE) supported by the National Science Foundation (NSF) as well as the Hera supercomputer of NOAA. This work is the first author's M.S. thesis at the Pennsylvania State University.

Data availability statement. WSR-88D radar observations are freely available from the National Center for Environmental Information. *GOES-16* satellite observations are freely available from the Comprehensive Large Array Data Stewardship System (CLASS) of NOAA. Conventional observations are freely available from the University Corporation for Atmospheric Research (UCAR)'s Research Data Archive. The GSI-EnKF data assimilation system is available from the Developmental Testbed Center (DTC) of UCAR, and the WRF-ARW data are available from NCAR. NEXRAD radar mosaic data are available from the Iowa Environmental Mesonet. West Texas Mesonet data are available from Synoptic Data. Oklahoma Mesonet data are provided courtesy of the Oklahoma Mesonet, which is jointly operated by Oklahoma State University and the University of Oklahoma. Continued funding of the network is provided by the taxpayers of Oklahoma. The numerical experiments can be shared upon request to the authors.

REFERENCES

Aksoy, A., D. C. Dowell, and C. A. Snyder, 2009: A multicase comparative assessment of the ensemble Kalman filter for the assimilation of radar observations. Part I: Storm-scale analyses. *Mon. Wea. Rev.*, **137**, 1805–1824, https://doi.org/10.1175/2008MWR2691.1.

Anderson, J. L., and S. L. Anderson, 1999: A Monte Carlo implementation of the nonlinear filtering problem to produce ensemble assimilations and forecasts. *Mon. Wea. Rev.*, **127**,

2741–2758, https://doi.org/10.1175/1520-0493(1999)127<2741:AMCIOT>2.0.CO;2.

Banghoff, J. R., D. J. Stensrud, and M. R. Kumjian, 2018: Convective boundary layer depth estimation from S-band dual-polarization radar. *J. Atmos. Oceanic Technol.*, **35**, 1723–1733, https://doi.org/10.1175/JTECH-D-17-0210.1.

Benjamin, S. G., G. A. Grell, J. M. Brown, T. G. Smirnova, and R. Bleck, 2004: Mesoscale weather prediction with the RUC hybrid isentropic-terrain-following coordinate model. *Mon. Wea. Rev.*, **132**, 473–494, https://doi.org/10.1175/1520-0493(2004)132<0473:MWPWTR>2.0.CO;2.

——, and Coauthors, 2016: A North American hourly assimilation and model forecast cycle: The Rapid Refresh. *Mon. Wea. Rev.*, **144**, 1669–1694, https://doi.org/10.1175/MWR-D-15-0242.1.

Bright, D. R., and S. L. Mullen, 2002: The sensitivity of the numerical simulation of the southwest monsoon boundary layer to the choice of PBL turbulence parameterization in MM5. *Wea. Forecasting*, **17**, 99–114, https://doi.org/10.1175/1520-0434(2002)017<0099:TSOTNS>2.0.CO;2.

Brock, F. V., K. C. Crawford, R. L. Elliott, G. W. Cuperus, S. J. Stadler, H. L. Johnson, and M. D. Eilts, 1995: The Oklahoma Mesonet: A technical overview. *J. Atmos. Oceanic Technol.*, **12**, 5–19, https://doi.org/10.1175/1520-0426(1995)012<0005:TOMATO>2.0.CO;2.

Brooks, H. E., C. A. Doswell III, and J. Cooper, 1994: On the environments of tornadic and nontornadic mesocyclones. *Wea. Forecasting*, **9**, 606–618, https://doi.org/10.1175/1520-0434(1994)009<0606:OTEOTA>2.0.CO;2.

Browning, K. A., and R. Wexler, 1968: The determination of kinetic properties of a wind field using Doppler radar. *J. Appl. Meteor. Climatol.*, **7**, 105–113, https://doi.org/10.1175/1520-0450(1968)007<0105:TDOKPO>2.0.CO;2.

——, and Coauthors, 2007: The convective storm initiation project. *Bull. Amer. Meteor. Soc.*, **88**, 1939–1956, https://doi.org/10.1175/BAMS-88-12-1939.

Cintineo, R. M., J. A. Otkin, T. A. Jones, S. Koch, and D. J. Stensrud, 2016: Assimilation of synthetic GOES-R ABI infrared brightness temperatures and WSR-88D radar observations in a high-resolution OSSE. *Mon. Wea. Rev.*, **144**, 3159–3180, https://doi.org/10.1175/MWR-D-15-0366.1.

Crook, N. A., 1996: Sensitivity of moist convection forced by boundary layer processes to low-level thermodynamic fields. *Mon. Wea. Rev.*, **124**, 1767–1785, https://doi.org/10.1175/1520-0493(1996)124<1767:SOMCFB>2.0.CO;2.

——, and J. Sun, 2002: Assimilating radar, surface and profiler data for the Sydney 2000 forecast demonstration project. *J. Atmos. Oceanic Technol.*, **19**, 888–898, https://doi.org/10.1175/1520-0426(2002)019<0888:ARSAPD>2.0.CO;2.

Dang, R., X. Qiu, Y. Yang, and S. Zhang, 2022: Observation system simulation experiments (OSSEs) for assimilation of the planetary boundary-layer height (PBLH) using the EnSRF technique. *Quart. J. Roy. Meteor. Soc.*, **148**, 1184–1207, https://doi.org/10.1002/qj.4254.

Degelia, S. K., X. Wang, and D. J. Stensrud, 2019: An evaluation of the impact of assimilating AERI retrievals, kinematic profilers, rawinsondes, and surface observations on a forecast of a nocturnal convection initiation event during the PECAN field campaign. *Mon. Wea. Rev.*, **147**, 2739–2764, https://doi.org/10.1175/MWR-D-18-0423.1.

Dixon, M., Z. Li, H. Lean, N. Roberts, and S. Ballard, 2009: Impact of data assimilation on forecasting convection over the United Kingdom using a high-resolution version of the Met Office Unified Model. *Mon. Wea. Rev.*, **137**, 1562–1584, https://doi.org/10.1175/2008MWR2561.1.

Dowell, D. C., F. Zhang, L. J. Wicker, C. Snyder, and N. A. Crook, 2004: Wind and temperature retrievals in the 17 May 1981 Arcadia, Oklahoma, supercell: Ensemble Kalman filter experiments. *Mon. Wea. Rev.*, **132**, 1982–2005, https://doi.org/10.1175/1520-0493(2004)132<1982:WATRIT>2.0.CO;2.

Eilts, M. D., and S. D. Smith, 1990: Efficient dealiasing of Doppler velocities using local environment constraints. *J. Atmos. Oceanic Technol.*, **7**, 118–128, https://doi.org/10.1175/1520-0426(1990)007<0118:EDODVU>2.0.CO;2.

Evensen, G., 1994: Sequential data assimilation with a nonlinear quasi-geostrophic model using Monte Carlo methods to forecast error statistics. *J. Geophys. Res.*, **99**, 10 143–10 162, https://doi.org/10.1029/94JC00572.

Gallo, B. T., and Coauthors, 2017: Breaking new ground in severe weather prediction: The 2015 NOAA/Hazardous Weather Testbed Spring Forecasting Experiment. *Wea. Forecasting*, **32**, 1541–1568, https://doi.org/10.1175/WAF-D-16-0178.1.

Gao, J., M. Xue, A. Shapiro, and K. K. Droegemeier, 1999: A variational method for the analysis of three-dimensional wind fields from two Doppler radars. *Mon. Wea. Rev.*, **127**, 2128–2142, https://doi.org/10.1175/1520-0493(1999)127<2128:AVMFTA>2.0.CO;2.

Gaspari, G., and S. E. Cohn, 1999: Construction of correlation functions in two and three dimensions. *Quart. J. Roy. Meteor. Soc.*, **125**, 723–757, https://doi.org/10.1002/qj.49712555417.

Geer, A. J., and Coauthors, 2018: All-sky satellite data assimilation at operational weather forecasting centres. *Quart. J. Roy. Meteor. Soc.*, **144**, 1191–1217, https://doi.org/10.1002/qj.3202.

Grimsdell, A. W., and W. M. Angevine, 1998: Convective boundary layer height measurement with wind profiles and comparison to cloud base. *J. Atmos. Oceanic Technol.*, **15**, 1331–1338, https://doi.org/10.1175/1520-0426(1998)015<1331:CBLHMW>2.0.CO;2.

Han, Y., P. van Delst, Q. Liu, F. Weng, B. Yan, R. Treadon, and J. Derber, 2006: JCSDA Community Radiative Transfer Model (CRTM)—version 1. NOAA Tech. Rep. NESDIS 122, 40 pp., https://repository.library.noaa.gov/view/noaa/1157.

Houtekamer, P. L., and F. Zhang, 2016: Review of the ensemble Kalman filter for atmospheric data assimilation. *Mon. Wea. Rev.*, **144**, 4489–4532, https://doi.org/10.1175/MWR-D-15-0440.1.

Hu, J., N. Yussouf, D. D. Turner, T. A. Jones, and X. Wang, 2019: Impact of ground-based remote sensing boundary layer observations on short-term probabilistic forecasts of a tornadic supercell event. *Wea. Forecasting*, **34**, 1453–1476, https://doi.org/10.1175/WAF-D-18-0200.1.

Hu, M., M. Xue, and K. Brewster, 2006: 3DVAR and cloud analysis with WSR-88D level-II data for the prediction of the Fort Worth, Texas, tornadic thunderstorms. Part I: Cloud analysis and its impact. *Mon. Wea. Rev.*, **134**, 675–698, https://doi.org/10.1175/MWR3092.1.

Huang, Y., X. Wang, C. Kerr, A. Mahre, T.-Y. Yu, and D. Bodine, 2020: Impact of assimilating future clear-air radial velocity observations from phased-array radar on a supercell thunderstorm forecast: An observing system simulation experiment study. *Mon. Wea. Rev.*, **148**, 3825–3845, https://doi.org/10.1175/MWR-D-19-0391.1.

——, ——, A. Mahre, T.-Y. Yu, and D. Bodine, 2022: Impacts of assimilating future clear-air radial velocity observations from phased-array radar on convection initiation forecasts: An observing system simulation experiment study. *Mon. Wea. Rev.*, **150**, 1563–1583, https://doi.org/10.1175/MWR-D-21-0199.1.

Iacono, M. J., J. S. Delamere, E. J. Mlawer, M. W. Shephard, S. A. Clough, and W. D. Collins, 2008: Radiative forcing by long-lived greenhouse gases: Calculations with the AER radiative transfer models. *J. Geophys. Res.*, **113**, D13103, https://doi.org/10.1029/2008JD009944.

Johnson, A., X. Wang, J. R. Carley, L. J. Wicker, and C. Karstens, 2015: A comparison of multiscale GSI-based EnKF and 3DVar data assimilation using radar and conventional observations for midlatitude convective-scale precipitation forecasts. *Mon. Wea. Rev.*, **143**, 3087–3108, https://doi.org/10.1175/MWR-D-14-00345.1.

——, ——, and T. A. Jones, 2022: Impacts of assimilating GOES-16 ABI Channels 9 and 10 clear air and cloudy radiance observations with additive inflation and adaptive observation error in GSI-EnKF for a case of rapidly evolving severe supercells. *J. Geophys. Res. Atmos.*, **127**, e2021JD036157, https://doi.org/10.1029/2021JD036157.

Johnson, R. H., and B. E. Mapes, 2001: Mesoscale processes and severe convective weather. *Severe Convective Storms*, *Meteor. Monogr.*, No. 28, Amer. Meteor. Soc., 71–122, https://doi.org/10.1175/0065-9401-28.50.71.

Johns, R. H., and C. A. Doswell III, 1992: Severe local storms forecasting. *Wea. Forecasting*, **7**, 588–612, https://doi.org/10.1175/1520-0434(1992)007<0588:SLSF>2.0.CO;2.

Jones, T. A., D. J. Stensrud, L. J. Wicker, P. Minnis, and R. Palikonda, 2015: Simultaneous radar and satellite data storm-scale assimilation using an ensemble Kalman filter approach for 24 May 2011. *Mon. Wea. Rev.*, **143**, 165–194, https://doi.org/10.1175/MWR-D-14-00180.1.

——, K. Knopfmeier, D. Wheatley, G. Creager, P. Minnis, and R. Palikonda, 2016: Storm-scale data assimilation and ensemble forecasting with the NSSL experimental Warn-on-Forecast System. Part II: Combined radar and satellite data experiments. *Wea. Forecasting*, **31**, 297–327, https://doi.org/10.1175/WAF-D-15-0107.1.

——, and Coauthors, 2020: Assimilation of *GOES-16* radiances and retrievals into the Warn-on-Forecast System. *Mon. Wea. Rev.*, **148**, 1829–1859, https://doi.org/10.1175/MWR-D-19-0379.1.

Kain, J. S., and Coauthors, 2013: A feasibility study for probabilistic convection initiation forecasts based on explicit numerical guidance. *Bull. Amer. Meteor. Soc.*, **94**, 1213–1225, https://doi.org/10.1175/BAMS-D-11-00264.1.

Kerr, C. A., D. J. Stensrud, and X. Wang, 2019: Diagnosing convective dependencies on near-storm environments using ensemble sensitivity analyses. *Mon. Wea. Rev.*, **147**, 495–517, https://doi.org/10.1175/MWR-D-18-0140.1.

Kleist, D. T., D. F. Parrish, J. C. Derber, R. Treadon, W.-S. Wu, and S. Lord, 2009: Introduction of the GSI into the NCEP global data assimilation system. *Wea. Forecasting*, **24**, 1691–1705, https://doi.org/10.1175/2009WAF2222201.1.

Liu, H., M. Hu, G. Ge, C. Zhou, D. Stark, H. Shao, K. Newman, and J. Whitaker, 2018: Ensemble Kalman filter (EnKF) user's guide version 1.3. Developmental Testbed Center, 81 pp., https://dtcenter.org/sites/default/files/community-code/enkf/docs/users-guide/EnKF_UserGuide_v1.3.pdf.

Lock, N. A., and A. L. Houston, 2014: Empirical examination of the factors regulating thunderstorm initiation. *Mon. Wea. Rev.*, **142**, 240–258, https://doi.org/10.1175/MWR-D-13-00082.1.

Martin, W. J., and M. Xue, 2006: Initial condition sensitivity analysis of a mesoscale forecast using very large ensembles. *Mon. Wea. Rev.*, **134**, 192–207.

McCaul, E. W., Jr., and C. Cohen, 2002: The impact on simulated storm structure and intensity of variations in the mixed layer and moist layer depths. *Mon. Wea. Rev.*, **130**, 1722–1748, https://doi.org/10.1175/1520-0493(2002)130<1722:TIOSSS>2.0.CO;2.

McPherson, R. A., and Coauthors, 2007: Statewide monitoring of the mesoscale environment: A technical update on the Oklahoma Mesonet. *J. Atmos. Oceanic Technol.*, **24**, 301–321, https://doi.org/10.1175/JTECH1976.1.

Melnikov, V. M., R. J. Doviak, D. S. Zrnić, and D. J. Stensrud, 2011: Mapping Bragg scatter with a polarimetric WSR-88D. *J. Atmos. Oceanic Technol.*, **28**, 1273–1285, https://doi.org/10.1175/JTECH-D-10-05048.1.

——, ——, ——, and ——, 2013: Structures of Bragg scatter observed with the polarimetric WSR-88D. *J. Atmos. Oceanic Technol.*, **30**, 1253–1258, https://doi.org/10.1175/JTECH-D-12-00210.1.

Minamide, M., and F. Zhang, 2018: Assimilation of all-sky infrared radiances from *Himawari-8* and impacts of moisture and hydrometeor initialization on convection-permitting tropical cyclone prediction. *Mon. Wea. Rev.*, **146**, 3241–3258, https://doi.org/10.1175/MWR-D-17-0367.1.

——, and D. J. Posselt, 2022: Using ensemble data assimilation to explore the environmental controls on the initiation and predictability of moist convection. *J. Atmos. Sci.*, **79**, 1151–1169, https://doi.org/10.1175/JAS-D-21-0140.1.

Nakanishi, M., and H. Niino, 2006: An improved Mellor–Yamada Level 3 model: Its numerical stability and application to a regional prediction of advection fog. *Bound.-Layer Meteor.*, **119**, 397–407, https://doi.org/10.1007/s10546-005-9030-8.

——, and ——, 2009: Development of an improved turbulence closure model for the atmospheric boundary layer. *J. Meteor. Soc. Japan*, **87**, 895–912, https://doi.org/10.2151/jmsj.87.895.

NOAA/National Centers for Environmental Information, 2022: U.S. Billion-Dollar Weather and Climate Disasters. NOAA/National Centers for Environmental Information, accessed 27 June 2022, https://www.ncdc.noaa.gov/billions/.

Olson, J. B., J. S. Kenyon, W. A. Angevine, J. M. Brown, M. Pagowski, and K. Sušelj, 2019: A description of the MYNN-EDMF scheme and the coupling to other components in WRF-ARW. NOAA Tech. Memo. OAR GSD 61, 37 pp., https://doi.org/10.25923/n9wm-be49.

Ryzhkov, A., P. Zhang, H. Reeves, M. Kumjian, T. Tschallener, S. Trömel, and C. Simmer, 2016: Quasi-vertical profiles—A new way to look at polarimetric radar data. *J. Atmos. Oceanic Technol.*, **33**, 551–562, https://doi.org/10.1175/JTECH-D-15-0020.1.

Schmit, T. J., P. Griffith, M. M. Gunshor, J. M. Daniels, S. J. Goodman, and W. J. Lebair, 2017: A closer look at the ABI on the GOES-R series. *Bull. Amer. Meteor. Soc.*, **98**, 681–698, https://doi.org/10.1175/BAMS-D-15-00230.1.

Schroeder, J. L., W. S. Burgett, K. B. Haynie, I. Sonmez, G. D. Skwira, A. L. Doggett, and J. W. Lipe, 2005: The West Texas Mesonet: A technical overview. *J. Atmos. Oceanic Technol.*, **22**, 211–222, https://doi.org/10.1175/JTECH-1690.1.

Schwartz, C. S., 2017: A comparison of methods used to populate neighborhood-based contingency tables for high-resolution forecast verification. *Wea. Forecasting*, **32**, 733–741, https://doi.org/10.1175/WAF-D-16-0187.1.

——, and R. A. Sobash, 2017: Generating probabilistic forecasts for convection-allowing ensembles using neighborhood approaches: A review and recommendations. *Mon. Wea. Rev.*, **145**, 3397–3418, https://doi.org/10.1175/MWR-D-16-0400.1.

Skamarock, W. C., and Coauthors, 2008: A description of the Advanced Research WRF version 3. NCAR Tech. Note NCAR/TN-475+STR, 113 pp., https://doi.org/10.5065/D68S4MVH.

Snyder, C., and F. Zhang, 2003: Assimilation of simulated Doppler radar observations with an ensemble Kalman filter. *Mon. Wea. Rev.*, **131**, 1663–1677, https://doi.org/10.1175//2555.1.

Sobash, R. A., and D. J. Stensrud, 2015: Assimilating surface Mesonet observations with the EnKF to improve ensemble forecasts of convection initiation on 29 May 2012. *Mon. Wea. Rev.*, **143**, 3700–3725, https://doi.org/10.1175/MWR-D-14-00126.1.

Soler, T., and D. W. Eisemann, 1994: Determination of look angles to geostationary communication satellites. *J. Surv. Eng.*, **120**, 115–127, https://doi.org/10.1061/(ASCE)0733-9453(1994)120:3(115).

Stensrud, D. J., 1996: Effects of a persistent, midlatitude mesoscale region of convection on the large-scale environment during the warm season. *J. Atmos. Sci.*, **53**, 3503–3527, https://doi.org/10.1175/1520-0469(1996)053<3503:EOPMMR>2.0.CO;2.

——, and S. J. Weiss, 2002: Mesoscale model ensemble forecasts of the 3 May 1999 tornado outbreak. *Wea. Forecasting*, **17**, 526–543, https://doi.org/10.1175/1520-0434(2002)017<0526:MMEFOT>2.0.CO;2.

——, and Coauthors, 2009: Convective-scale Warn-on-Forecast System: A vision for 2020. *Bull. Amer. Meteor. Soc.*, **90**, 1487–1500, https://doi.org/10.1175/2009BAMS2795.1.

——, and Coauthors, 2013: Progress and challenges of Warn-on-Forecast. *Atmos. Res.*, **123**, 2–16, https://doi.org/10.1016/j.atmosres.2012.04.004.

Sun, J., 2005: Initialization and numerical forecasting of a supercell storm observed during STEPS. *Mon. Wea. Rev.*, **133**, 793–813, https://doi.org/10.1175/MWR2887.1.

——, and Y. Zhang, 2008: Analysis and prediction of a squall line observed during IHOP using multiple WSR-88D observations. *Mon. Wea. Rev.*, **136**, 2364–2388, https://doi.org/10.1175/2007MWR2205.1.

Tangborn, A., B. Demoz, B. J. Carroll, J. Santanello, and J. L. Anderson, 2021: Assimilation of lidar planetary boundary layer height observations. *Atmos. Meas. Tech.*, **14**, 1099–1110, https://doi.org/10.5194/amt-14-1099-2021.

Thompson, G., P. R. Field, R. M. Rasmussen, and W. D. Hall, 2008: Explicit forecasts of winter precipitation using an improved bulk microphysics scheme. Part II: Implementation of a new snow parameterization. *Mon. Wea. Rev.*, **136**, 5095–5115, https://doi.org/10.1175/2008MWR2387.1.

Tong, M., and M. Xue, 2005: Ensemble Kalman filter assimilation of Doppler radar data with a compressible nonhydrostatic model: OSS experiments. *Mon. Wea. Rev.*, **133**, 1789–1807, https://doi.org/10.1175/MWR2898.1.

Wang, X., and T. Lei, 2014: GSI-based four-dimensional ensemble-variational (4DEnsVar) data assimilation: Formulation and single-resolution experiments with real data for NCEP global forecast system. *Mon. Wea. Rev.*, **142**, 3303–3325, https://doi.org/10.1175/MWR-D-13-00303.1.

——, D. Parrish, D. Kleist, and J. Whitaker, 2013: GSI 3DVar-based ensemble-variational hybrid data assimilation for NCEP global forecast system: Single-resolution experiments. *Mon. Wea. Rev.*, **141**, 4098–4117, https://doi.org/10.1175/MWR-D-12-00141.1.

Weckwerth, T. M., and D. B. Parsons, 2006: A review of convection initiation and motivation for IHOP_2002. *Mon. Wea. Rev.*, **134**, 5–22, https://doi.org/10.1175/MWR3067.1.

Wheatley, D. M., K. H. Knopfmeier, T. A. Jones, and G. J. Creager, 2015: Storm-scale data assimilation and ensemble forecasting with the NSSL experimental Warn-on-Forecast System. Part I: Radar data experiments. *Wea. Forecasting*, **30**, 1795–1817, https://doi.org/10.1175/WAF-D-15-0043.1.

Whitaker, J. S., and T. M. Hamill, 2002: Ensemble data assimilation without perturbed observations. *Mon. Wea. Rev.*, **130**, 1913–1924, https://doi.org/10.1175/1520-0493(2002)130<1913:EDAWPO>2.0.CO;2.

Wilks, D. S., 2011: *Statistical Methods in the Atmospheric Sciences*. 3rd ed. International Geophysics Series, Vol. 100, Academic Press, 704 pp.

Wu, W.-S., R. J. Pursuer, and D. F. Parrish, 2002: Three-dimensional variational analysis with spatially inhomogeneous covariances. *Mon. Wea. Rev.*, **130**, 2905–2916, https://doi.org/10.1175/1520-0493(2002)130<2905:TDVAWS>2.0.CO;2.

Xu, Q., C.-J. Qiu, H.-D. Gu, and J.-X. Yu, 1995: Simple adjoint retrievals of microburst winds from single-Doppler radar data. *Mon. Wea. Rev.*, **123**, 1822–1833, https://doi.org/10.1175/1520-0493(1995)123<1822:SAROMW>2.0.CO;2.

Yussouf, N., E. R. Mansell, L. J. Wicker, D. M. Wheatley, and D. J. Stensrud, 2013: The ensemble Kalman filter analyses and forecasts of the 8 May 2003 Oklahoma City tornadic supercell storm using single- and double-moment microphysics schemes. *Mon. Wea. Rev.*, **141**, 3388–3412, https://doi.org/10.1175/MWR-D-12-00237.1.

——, D. C. Dowell, L. J. Wicker, K. H. Knopfmeier, and D. M. Wheatley, 2015: Storm-scale data assimilation and ensemble forecasts for the 27 April 2011 severe weather outbreak in Alabama. *Mon. Wea. Rev.*, **143**, 3044–3066, https://doi.org/10.1175/MWR-D-14-00268.1.

Zhang, F., C. Snyder, and J. Sun, 2004: Impacts of initial estimate and observation availability on convective-scale data assimilation with an ensemble Kalman filter. *Mon. Wea. Rev.*, **132**, 1238–1253, https://doi.org/10.1175/1520-0493(2004)132<1238:IOIEAO>2.0.CO;2.

——, Y. Weng, J. A. Sippel, Z. Meng, and C. H. Bishop, 2009: Cloud-resolving hurricane initialization and prediction through assimilation of Doppler radar observations with an ensemble Kalman filter. *Mon. Wea. Rev.*, **137**, 2105–2125, https://doi.org/10.1175/2009MWR2645.1.

——, M. Minamide, and E. E. Clothiaux, 2016: Potential impacts of assimilating all-sky infrared satellite radiances from GOES-R on convection-permitting analysis and prediction of tropical cyclones. *Geophys. Res. Lett.*, **43**, 2954–2963, https://doi.org/10.1002/2016GL068468.

Zhang, Y., F. Zhang, and D. J. Stensrud, 2018: Assimilating all-sky infrared radiances from *GOES-16* ABI using an ensemble Kalman filter for convection-allowing severe thunderstorms prediction. *Mon. Wea. Rev.*, **146**, 3363–3381, https://doi.org/10.1175/MWR-D-18-0062.1.

——, D. J. Stensrud, and F. Zhang, 2019: Simultaneous assimilation of radar and all-sky satellite infrared radiance observations for convection-allowing ensemble analysis and prediction of severe thunderstorms. *Mon. Wea. Rev.*, **147**, 4389–4409, https://doi.org/10.1175/MWR-D-19-0163.1.

——, E. E. Clothiaux, and D. J. Stensrud, 2022: Correlation structures between satellite all-sky infrared brightness temperatures and the atmospheric state at storm scales. *Adv. Atmos. Sci.*, **39**, 714–732, https://doi.org/10.1007/s00376-021-0352-3.

Zou, X., F. Weng, B. Zhang, L. Lin, Z. Qin, and V. Tallapragada, 2013: Impacts of assimilation of ATMS data in HWRF on track and intensity forecasts of 2012 four landfall hurricanes. *J. Geophys. Res. Atmos.*, **118**, 11 558–11 576, https://doi.org/10.1002/2013JD020405.